Journal of Sound and Vibration 626 (2026) 119617

Contents lists available at ScienceDirect

Journal of Sound and Vibration

journal homepage: www.elsevier.com/locate/jsvi

Bouc-Wen modelling of asymmetric Stockbridge damper for the wind-induced vibration control of suspension bridge hangers

G. Bacci [a,*], Ø.W. Petersen [a], V. Denoël [b], O. Øiseth [a]

[a] NTNU, Norwegian University of Science and Technology, 7491, Trondheim, Norway
[b] ULiège, University of Liège, 4000, Liège, Belgium

ARTICLE INFO

Keywords:
Stockbridge
Bouc-Wen
Vortex-induced vibration
Nonlinear dynamics
Hanger vibration
Suspension bridge

ABSTRACT

Stockbridge dampers are traditionally employed in overhead transmission lines, but their application has recently expanded to suspension bridge hangers. In this context, their increased size, asymmetric configuration, vertical installation, and absence of dedicated design standards present new challenges in understanding their dynamic behaviour. Proper characterisation is essential to correctly dimension the device and determine its optimal placement on the structure. This study addresses these challenges by presenting a four-degree-of-freedom nonlinear model of an asymmetric Stockbridge damper using the Bouc-Wen hysteretic formulation to capture the messenger cables' amplitude-dependent stiffness and energy dissipation. The model is calibrated and validated against experimental tests conducted on dampers equal to the ones installed on the hangers of the Hålogaland long-span suspension bridge. Unlike impedance-based black-box models, the proposed framework provides a physically consistent representation that can be directly embedded into system-level simulations of hanger-damper dynamics. The present framework can accurately reconstruct both the overall transmitted force and the internal dynamics, in close agreement with the measured responses across varying amplitudes and frequencies. In comparison to existing formulations developed for overhead line dampers, it requires no additional parameters but more effectively captures the amplitude-dependent variation of the damper's dynamic behaviour, providing improved accuracy in representing its nonlinear characteristics.

1. Introduction

Stockbridge dampers are commonly employed to reduce vortex-induced vibrations in overhead electrical transmission lines and other cable-like structures subjected to wind forces. In recent years, their use has expanded to hangers of suspension bridges-an application that presents new challenges due to the larger size of the dampers, the asymmetry of the attached masses, their installation in a vertical configuration, and the absence of dedicated design standards or installation guidelines. Recent contributions have reported cases of premature device failure before the expected design life on the Çanakkale Bridge in Turkey [1] and on the Hålogaland bridge in Norway [2]. The cause of failure is often linked to a fatigue fracture in the messenger cable close to the clamp or one of the masses. The fact that dampers are failing in these applications while being tested and designed according to standards intended for a different context [3,4], highlights the need for further research and advancements in this field.

* Corresponding author.
E-mail addresses: giacomo.bacci@ntnu.no (G. Bacci), oyvind.w.petersen@ntnu.no (Ø.W. Petersen), v.denoel@uliege.be (V. Denoël), ole.oiseth@ntnu.no (O. Øiseth).
URL: https://www.ntnu.edu/kt (G. Bacci)

https://doi.org/10.1016/j.jsv.2025.119617
Received 17 October 2025; Received in revised form 12 December 2025; Accepted 16 December 2025
Available online 19 December 2025

(a) (b)

Fig. 1. a) Two Stockbridge dampers installed on a hanger of the Hålogaland bridge in Narvik, Norway. b) Test sample of a Stockbridge damper.

First introduced by Stockbridge in 1925 [5], this type of device has undergone numerous improvements and developments over the years. The asymmetric version treated in this paper originates from the work of Claren and Diana in 1969 [6]. A typical Stockbridge damper comprises a short steel strand, a clamp that fixes the mid-point of the strand to the structure needing additional damping, and two masses fixed to each end of the strand, see Fig. 1b. This strand cable is commonly referred to as "messenger cable" or "messenger strand" because Stockbridge's original prototype employed the type of cable used, at that time, for overhead telephone lines [7,8]. The damper acts as a supplementary dynamic system that aids in dissipating energy. When the damper is excited by the clamp motion, the messenger cable functions as a flexible cantilever beam with lumped masses at its ends represented by a mass m and a rotational inertia J. If the system behaves linearly, each of the masses exhibits two vibration modes in the plane. However, unlike a linear cantilever, the actual behaviour of the messenger cable is nonlinear and quasi-linear "modes" or *modality* of vibration that depend on amplitude are observed [9]. Indeed, unlike traditional tuned mass dampers, which exhibit linear damping characteristics, Stockbridge dampers demonstrate nonlinear and hysteretic behaviour due to the complex mechanical behaviour of the messenger cable. During the rotational and translational movement of the masses, the messenger cable bends, and the relative movement between its individual wires occurs. The extent of this inter-wire slip increases with the vibration amplitude, dissipating energy through friction, inherently leading to a nonlinear dynamic response. As a result, both the damping efficiency and dynamic stiffness of the damper depend on the amplitude of the vibration that is transmitted to the damper through the clamp motion. The amplitude-dependent behaviour of Stockbridge dampers has long been recognised in the literature on overhead transmission lines. Classical studies describe the messenger cable as a nonlinear, hysteretic bending element whose effective stiffness decreases with increasing curvature or clamp motion amplitude [4,7,10,11]. This softening results from inter-strand slip within the spiral-strand messenger cable and leads to a reduction in the apparent bending stiffness at larger vibration amplitudes. In these works, the variation of effective stiffness is often inferred indirectly from measured shear forces and bending moments at the clamp, revealing a transition from a high-stiffness regime at small amplitudes to a markedly lower stiffness when macro-slip develops. Although these studies primarily focus on dampers mounted on overhead conductors, they highlight that bending stiffness nonlinearity is an intrinsic feature of Stockbridge dampers and the primary cause of their amplitude-dependent dynamic response.

The nonlinear nature of Stockbridge dampers is a key factor in their ability to mitigate wind-induced vibrations in cables effectively. This nonlinearity helps overcome detuning issues that commonly affect conventional linear tuned mass dampers, which can arise from variations in the damper's mechanical properties or shifts in operational conditions over time [12]. In addition, this nonlinearity lets the device dissipate energy over a broad band of frequencies rather than at a single tuned frequency. This is an indispensable advantage given the many closely spaced vibration modes found in cable structures. Despite the significant impact of the messenger cable's hysteretic bending behaviour on the overall performance of Stockbridge dampers, limited research has been dedicated to characterising this phenomenon. Earlier works by Pivovarov and Vinogradov [13] modelled the messenger cable as a single-degree-of-freedom system, employing the phenomenological hysteresis model introduced by Bouc [14] and later expanded by Wen [15], in the following referenced as the Bouc-Wen model. The Bouc-Wen model offers a framework based on differential equations for simulating nonlinear constitutive behaviour. It uses a history variable to account for hysteresis and asymmetrical responses, making it a flexible tool in structural dynamics. While this approach could replicate a range of hysteresis patterns, its primary limitation was the ability to capture only a single degree of freedom due to the simplifications of the model.

Efforts have been made to develop a physics-based analytical model of the spiral strand [16]. However, the challenge of achieving a sufficiently accurate description of the radial contact between each strand of the messenger cable has made the model difficult to tune and implement in practice. More recent approaches leverage Euler-Bernoulli beam theory to provide another representation of the system's modal properties. Sauter and Hagedorn [17] modelled the messenger cable as a nonlinear beam with its

moment-curvature relationship described by the Masing hysteresis model. The model parameters were identified through static testing, and its numerical predictions were validated against experimental results obtained from a shaker table test of a Stockbridge damper prototype, demonstrating promising agreement. Building on the extensive experimental work of Sauter [18], Foti et al. [19] incorporated the Bouc-Wen model to describe the nonlinear static bending behaviour of the section of the messenger cable.

Further advancements have been made using finite element modelling. Langlois and Legeron [20], as well as Barbieri et al. [9,21,22], implemented nonlinear beam element models incorporating phenomenological hysteretic behaviour, with model parameters derived from static and dynamic experimental tests. More recently, Luo [23] developed a full-scale nonlinear finite element model using 3D solid elements. This approach allows for a detailed representation of local contact conditions between the wires of the messenger cable and between the clamp and cable, revealing the significant influence of these localised interactions on the damper's overall dynamic response. However, while these full-scale 3D finite element models offer high accuracy, they are computationally demanding and require careful calibration, especially given the presence of numerous nonlinear contact interfaces.

In more recent studies, Foti et al. [24] revisited Pivovarov's work using a Bouc-Wen model with a minimal parameter set. Bogani et al. [25] further refined this approach to extend the single-degree-of-freedom formulation to account for the rotational motion of the inertial masses. To date, most research on modelling Stockbridge dampers has focused on their application in mitigating wind-induced vibrations in overhead transmission lines. However, in recent years, their use has been expanded to other structural applications, such as mitigating vortex-induced vibrations in suspension bridge hangers [26] and cable-stayed bridge cables [27,28]. Compared to applications in overhead transmission lines, these dampers are often larger, asymmetric, and designed to operate over a broader frequency range. Additionally, they are frequently installed in a vertical orientation. However, the codes currently used to characterise and test these devices for bridge applications are still those originally developed for overhead power lines [3,4], which may not fully account for the unique demands of bridge structures. Moreover, previous studies on the optimal tuning of Stockbridge dampers have shown that their dynamic efficiency strongly depends on the boundary conditions and installation configuration of the cable-damper system, with the optimum impedance varying between suspension and dead-end spans [29].

Notably, most of the models mentioned above have been developed for symmetric dampers for high-voltage transmission lines applications and validated through experiments considering horizontally mounted dampers. As a result, these models are often formulated for only half of the damper to exploit symmetry and, at best, experimentally identify the double-peak frequency response relating the damper's input motion and the output force exerted on the structure [17,19,23]. In these studies, the analysed motion is typically assumed to be planar, as the most significant cable vibrations requiring damping are caused by vortex-induced vibration, which occurs predominantly in a plane perpendicular to the wind direction. In practice, these models usually capture only the first, or at most the second, peak of this transfer function, corresponding respectively to the lateral translation and, in some cases, rotation of the mass in the modelled half-damper. Because the damper is symmetric, it is assumed that its dynamic behaviour is also symmetric, and the force generated by one mass is doubled to estimate the total damping force.

In the present study, we build upon the work of Bogani [25,30], who employed a two-degree-of-freedom reduced hysteresis model to describe the dynamics of a symmetric Stockbridge damper used in overhead line applications. The hysteretic restoring force of the messenger cable was represented using a Bouc-Wen model with a minimal parameter formulation. While Bogani validated his model using literature data for horizontally tested power line dampers, here we develop a dedicated laboratory setup that allows for shaker excitation of a vertically mounted asymmetric Stockbridge damper, replicating the orientation and boundary conditions of field installations on a vertical hanger. Specifically, we extend Bogani's approach by developing a four-degree-of-freedom model, adapted for an asymmetric Stockbridge damper designed to mitigate wind-induced vibrations in suspension bridge hangers. Beyond the increased number of degrees of freedom, the proposed model is based on a collection of independent 1-DOF Bouc-Wen models representing some generalised coordinates. Unlike other available models in the literature, these coordinates are obtained by linear transformation of the physical coordinates (tip displacement and rotation) of the Stockbridge masses. This modelling option allows working with a simple model, with possible physical interpretation of the model parameters, and offers the possibility of identifying the parameters associated with each resonance independently, which significantly simplifies the calibration process. The model parameters are identified experimentally using this vertical setup, and the model performance is assessed with both monoharmonic and multiharmonic forcing time histories.

The model is finally reduced to a two-degree-of-freedom version and compared against the models available in literature by Bogani [25] and Sauter [18], for overhead power line dampers.

2. Analytical model of the Stockbridge damper

2.1. Equations of motion

In the present work, we consider an asymmetric Stockbridge damper, where the asymmetry arises from differences in the lengths of the messenger cables and in the masses of the attached weights. Fig. 1b shows a picture of the device, and the geometric parameters are given in Table 1.

The damper is installed vertically on the hangers of the bridge, with the larger mass on the bottom, and the clamp connected to the hanger by a bracket (Fig. 1a). The damper and the hanger form a combined dynamic system, where the hanger's movement drives the motion of the damper's masses, leading to energy dissipation. The interaction between the hanger and the damper occurs through the transmission of a force $F_c(t)$ and a moment $M_c(t)$ through the clamp. Assuming that the clamp and the masses are rigid, the damper can be modelled as three bodies connected by a set of nonlinear spring-dampers [19]. In the present work, only the horizontal degree of freedom of the clamp, denoted as $y_c(t)$, is considered. This assumption is justified by the fact that the dampers

Table 1
Geometric parameters of the tested Stockbridge dampers.

Parameter	Symbol	Value
Top mass	m_1	4.6 [kg]
Bottom mass	m_2	7.7 [kg]
Mass of the clamp	m_c	0.931 [kg]
Rotational inertia of top mass (about centroid)	J_1	0.02145 [kg·m^2]
Rotational inertia of bottom mass (about centroid)	J_2	0.05234 [kg·m^2]
Distance from tip of messenger cable to centroid (top mass)	$e_{G,1}$	0.034 [m]
Distance from tip of messenger cable to centroid (bottom mass)	$e_{G,2}$	0.040 [m]
Length of top messenger cable	L_1	0.240 [m]
Length of bottom messenger cable	L_2	0.274 [m]
Diameter of messenger cable	D_{cable}	0.017 [m]

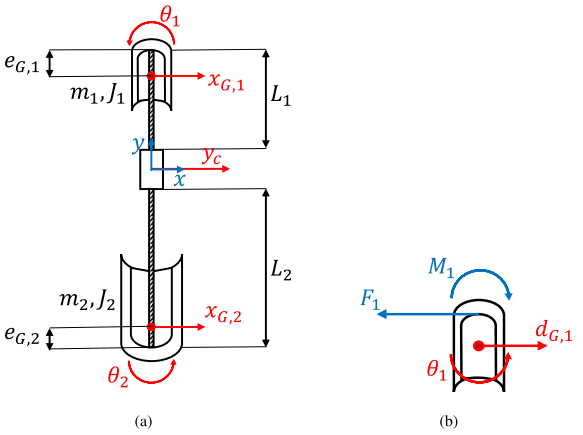

Fig. 2. a) Scheme of a Stockbridge damper with four degrees of freedom. b) Reaction forces of the messenger cable and the degrees of freedom of the top mass at their interface connection.

are deliberately installed away from the nodal points of the hanger modes corresponding to the frequencies where the damper is most effective in dissipating energy. In these regions, the rotational component at the clamp is negligible, and the horizontal translation of the clamp is expected to govern the excitation of the damper. We will focus on the modelling of the transmitted force F_c, which represents the main contribution to energy dissipation when the damper is positioned away from a node. Finally, the formulation is restricted to two dimensions, as vortex-induced vibrations in hangers occur predominantly in a vertical plane perpendicular to the wind direction.

A schematic representation of the damper and its associated degrees of freedom is provided in Fig. 2a. The in-plane dynamics of each mass can be completely described by specifying the horizontal translation $x_{Gi}(t)$ and rotation $\theta_i(t)$ of its centroid. In the following sections, any variable that may refer to either mass of the damper is distinguished by the subscript i, with $i = 1$ denoting the upper (smaller) mass and $i = 2$ denoting the lower (larger) mass. The mass of the messenger cable is neglected in the model, as it is small compared to the two masses. Since energy dissipation occurs through friction within the messenger cables-and this friction depends on the cables' deformation-it is convenient to introduce the relative displacement between the centroid of the masses and the clamp, denoted by $d_{Gi}(t)$ in the equations. The horizontal displacement of the centroid i can then be written as

$$x_{Gi} = y_c + d_{Gi} \tag{1}$$

The equations of motion of each of the two masses can be obtained via Hamilton's variational principle applied to nonholonomic, discrete dynamic systems [31]. The total variation of the action integral over two generic time instants t_1 and t_2 must be zero, as shown in Eq. (2), where δT_i is the variation of kinetic energy of the i^{th} inertial mass and δW_i is the work done by the restoring force of the messenger cable on the i^{th} mass.

$$\int_{t_2}^{t_1} (\delta T_i + \delta W_i) dt = 0 \tag{2}$$

The kinetic energy of each of the masses can be expressed as in Eq. (3), accounting for both translational inertia, with the mass m_i, and rotational inertia, with the mass moment of inertia with respect to the centroid J_i. However, because the energy dissipation depends on the deformation of the messenger cable, it is helpful to express the equations in terms of the relative displacement of the centroid with respect to the clamp ($d_{Gi}(t)$) and the rotation of the mass ($\theta_i(t)$). Therefore, with the use of Eq. (1), the kinetic energy

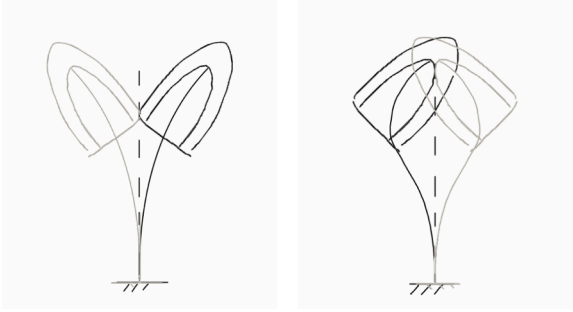

Fig. 3. Schematic of the first (a) and second (b) deformation shapes at resonance of one messenger cable.

can be expressed as

$$T_i = \frac{1}{2} m_i \dot{x}_{Gi}^2 + \frac{1}{2} J_i \dot{\theta}_i^2 = \frac{1}{2} m_i (\dot{y}_c + \dot{d}_{Gi})^2 + \frac{1}{2} J_i \dot{\theta}_i^2 \tag{3}$$

The restoring forces acting on the inertial masses are the shear force F_i and the moment M_i acting at the cable tip, as shown in Fig. 2b. The corresponding virtual work contribution for the i^{th} mass is expressed as

$$\delta W_i = -F_i \delta d_{Gi} - M_i \delta \theta_i + \eta_i e_{Gi} F_i \delta \theta_i \tag{4}$$

which is used within the variational framework to derive the equations of motion. Here $\eta_i = (-1)^{i+1}$ accounts for the relative orientation of each mass, ensuring a correct sign for the moment arm of the horizontal force F_i, while e_{Gi} is the distance from the centroid of mass i to the tip of the corresponding messenger cable. By enforcing the condition expressed in Eq. (2), that the total action integral is zero over any time interval, the fundamental lemma of the calculus of variations can be applied, leading to the set of Euler-Lagrange equations:

$$\frac{d}{dt}\left(\frac{\partial T_i}{\partial \dot{d}_i}\right) + F_i = 0 \tag{5a}$$

$$\frac{d}{dt}\left(\frac{\partial T_i}{\partial \dot{\theta}_i}\right) + M_i = 0 \tag{5b}$$

Taking the derivative of the kinetic energy in Eq. (3) and substituting in Eq. (5), the following system of equations is obtained:

$$m_i \ddot{d}_{Gi} + F_i = -m_i \ddot{y}_c \tag{6a}$$

$$J_i \ddot{\theta}_i + M_i - \eta_i e_{Gi} F_i = 0 \tag{6b}$$

These equations represent the dynamics of the i^{th} mass as the equilibrium between the inertial forces and the nonlinear reaction forces of the i^{th} messenger cable.

In the following Section 2.2, the nonlinear behaviour of the Stockbridge damper is modelled using the well-known Bouc-Wen formulation [14]. The original model was developed for a single internal degree of freedom and has since been extended to multiple degrees of freedom. However, such extensions often face difficulties, particularly in representing coupling effects through additional nonlinear terms. In the present work, we deliberately avoid these complications by not adopting a full four-dimensional Bouc-Wen model. While such an approach would be more general, it would also be unnecessarily complex for the purposes of the current study. Indeed, a Stockbridge damper is designed to provide efficiency over a broad frequency range, with distinct resonances, with very little possible interaction. These resonances correspond to states in which the damper masses vibrate with large amplitudes, involving various combinations of tip displacements and rotations. A scheme of the first two resonance deformation shapes for one of the masses of the damper is shown in Fig. 3. Drawing inspiration from modal analysis, the proposed model employs four uncoupled Bouc-Wen systems defined in generalised coordinates u_{1i} [m] and u_{2i} [m]. These generalised coordinates are related to the physical quantities d_{Gi} and θ_i through a simple linear transformation, again inspired by the use of modal coordinates in structural dynamics. Through the following derivations, it is shown that this model is simple and versatile enough to capture the essential features of an asymmetric Stockbridge damper's dynamics. The relation between the generalized coordinates $u_{1,i}$ and $u_{2,i}$ and the physical quantities d_{Gi} and θ_i is defined as

$$\begin{pmatrix} d_{Gi} \\ \theta_i \end{pmatrix} = \begin{bmatrix} 1 & a_i \\ b_i & 1 \end{bmatrix} \begin{pmatrix} u_{1,i} \\ u_{2,i} \end{pmatrix} = \phi_i \begin{pmatrix} u_{1,i} \\ u_{2,i} \end{pmatrix} \tag{7}$$

where ϕ_i is the transformation matrix, and it is expressed as a function of two parameters a_i [m] and b_i [rad/m], which are related to the ratio of displacement and rotation of the masses of the damper in the resonance states. In this way, Eq. (6) can be rewritten in terms of the new generalised coordinates $u_{1,i}$ [m] and $u_{2,i}$ [m] as

$$\phi_i^T \begin{bmatrix} m_i & \\ & J_i \end{bmatrix} \phi_i \begin{pmatrix} \ddot{u}_{1,i} \\ \ddot{u}_{2,i} \end{pmatrix} = -\begin{pmatrix} \tilde{F}_{1,i} \\ \tilde{F}_{2,i} \end{pmatrix} + \phi_i^T \begin{pmatrix} -m\ddot{y}_c \\ 0 \end{pmatrix} \tag{8}$$

here $\tilde{F}_{1,i}(u_{1,i}, \dot{u}_{1,i})$ [N] and $\tilde{F}_{2,i}(u_{2,i}, \dot{u}_{2,i})$ [N] denote the nonlinear restoring forces expressed in the transformed coordinates acting on mass i. A suitable expression for these forces will be the subject of Section 2.2. Assuming a model for the nonlinear forces is established and the input clamp motion is known, the system is numerically integrated, and the time history of the generalised variables $u_{1,i}$ and $u_{2,i}$ is obtained. The time history of the state variables d_{Gi} and θ_i is then reconstructed by Eq. (7).

Once the dynamics of each of the masses is calculated, the force acting at the clamp F_c is determined via an equilibrium (see Fig. 2b). The total force exchanged by the damper to the hanger cable is the sum of the inertial force of the clamp and the contributions coming from the internal reaction forces of the two messenger cables:

$$F_c = m_c \ddot{y}_c - \left(F_1 + F_2\right) \tag{9}$$

The time history of the internal reaction forces F_i and M_i is reconstructed from the nonlinear generalised reaction forces as

$$\begin{pmatrix} F_i \\ M_i \end{pmatrix} = \left(\phi_i^T \begin{bmatrix} 1 & 0 \\ \eta e_{Gi} & 1 \end{bmatrix} \right)^{-1} \begin{pmatrix} \tilde{F}_{1,i} \\ \tilde{F}_{2,i} \end{pmatrix} \tag{10}$$

which can also be rewritten into Eq. (11), to highlight the effect of the scaling parameters a_i and b_i in weighting the contribution of each of the two nonlinear generalised reaction forces for each internal reaction force F_i.

$$F_i = \frac{1}{1 - a_i b_i} \tilde{F}_{1,i} - \frac{b_i}{1 - a_i b_i} \tilde{F}_{2,i} \tag{11}$$

2.2. The Bouc-Wen hysteresis model

In this section, an expression for the nonlinear generalised reaction forces $\tilde{F}_{1,i}$ and $\tilde{F}_{2,i}$ of each messenger cable is derived. A possible solution to express the nonlinear hysteretic behaviour of the messenger cables is to use the hysteretic Bouc-Wen model. Different formulations of the original Bouc-Wen model are present in the literature [32–34]. The one used in this work originates from the work by Ikhouane and coworkers [35,36] and it is defined by the following system of equations:

$$\tilde{F}_{ji} = k_{ji}^{\min} u_{ji} + \left(k_{ji}^{\max} - k_{ji}^{\min}\right) c_{ji} z_{ji} \tag{12a}$$

$$\dot{z}_{ji} = \frac{1}{c_{ji}} \left[\dot{u}_{ji} - \sigma |\dot{u}_{ji}| |z_{ji}|^{n-1} z_{ji} + (\sigma - 1) \dot{u}_{ji} |z_{ji}|^n\right] \tag{12b}$$

In Eq. (12a), the generic restoring force $\tilde{F}_{ji}$ is expressed as a function of the generalised coordinate u_{ji} and the hysteretic variable z_{ji}, where $i \in \{1,2\}$ is the mass index and $j \in \{1,2\}$ is the generalised coordinate index. The dynamics of the dimensionless hysteretic variable z_{ji} is ruled by the first-order nonlinear differential equation in Eq. (12b). The parameters of the model $k_{ji}^{\min}$ and $k_{ji}^{\max}$ represent the initial and post-yielding generalised stiffness of the system. The parameter c_{ji} represents the generalised coordinate displacement at which the system starts yielding. The unit of measurement of $k_{ji}^{\min}$, $k_{ji}^{\max}$ will be in [N/m] and c_{1i} in [m]. As shown in the scheme in Fig. 4a, when the amplitude of the displacement $A_{u_{ji}} = \max_t \left|u_{ji}\right|$ is smaller than c_{ji}, the system behaves linearly with stiffness $k_{ji}^{\max}$ and little energy is dissipated. Conversely, when the displacement amplitude $A_{u_{ji}}$ exceeds c_{ji}, the system can reach states with a stiffness as low as the lower stiffness $k_{ji}^{\min}$. However, the variation in the effective stiffness $k_{eff} = F_{\max}/u_{\max}$ is gradual rather than abrupt, as illustrated in Fig. 4b, which also shows how increasing the parameter c_{ji} shifts the amplitude at which this transition begins. The degree of nonlinearity of the system is governed by the difference between $k_{ji}^{\min}$ and $k_{ji}^{\max}$: the larger this difference, the stronger the hysteretic effects and the greater the variation in the system's dynamic behaviour with changes in input amplitude. Fig. 4c presents an example of a hysteresis loop in the force-displacement plane obtained with this model. An increase in $k_{ji}^{\max}$ makes the loop wider, whereas an increase in $k_{ji}^{\min}$ makes the loop narrower and more vertical. The parameters σ and n are non-dimensional parameters controlling the shape of the transition between the two linear parts of the hysteresis cycle. For the application to one and two degrees of freedom models of Stockbridge dampers, it has already been shown that the number of parameters to train can be successfully reduced by setting $\sigma = 1$ and $n = 1$ [24]. This leads to the simpler formulation of the differential equation for the hysteretic variable:

$$\dot{z}_{ji} = \frac{1}{c_{ji}} \psi(\dot{u}_{ji}, z_{ji}) \dot{u}_{ji} \tag{13}$$

where $\psi(\dot{u}_{ji}, z_{ji}) = 1 - \mathrm{sgn}(\dot{u}_{ji}) z_{ji}$. To define a Bouc-Wen framework, three parameters, for each (j,i) combination, will have to be set: $k_{ji}^{\min}$, $k_{ji}^{\max}$ and c_{ji}. Therefore, with two degrees of freedom for each mass ($j \in \{1,2\}$) and an asymmetric Stockbridge damper ($i \in \{1,2\}$), a total of 12 parameters need to be determined.

It should be noted that the numerical values of the identified model parameters also depend on elements a_i and b_i of the transformation matrix ϕ. Different choices of the factors a_i and b_i will therefore lead to different parameter values. They are therefore also adjusted from the experimental data.

To numerically integrate the equations of motion, the system is recast in state-space form and augmented with the hysteretic internal variables defined by the Bouc-Wen model of the generalised reaction forces. For the i^{th} mass, the transformed state vector is

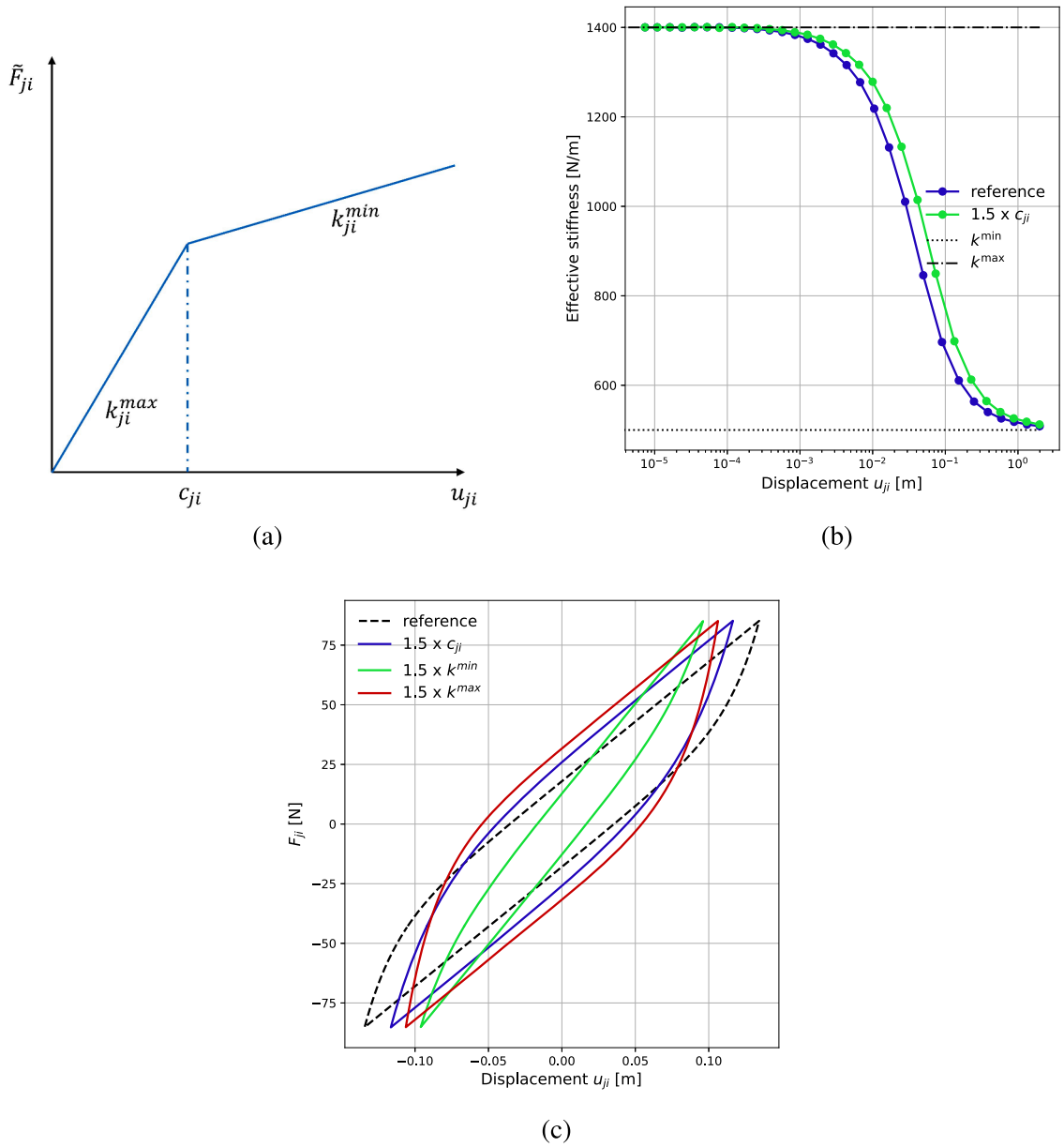

Fig. 4. a) Typical loading force-displacement diagram of a stranded cable. b) Variation of effective stiffness $k_{eff} = F_{\max}/u_{\max}$ with an increase in displacement amplitude (reference: $k_{ji}^{\min} = 500$ N/m, $k_{ji}^{\max} = 1400$ N/m and $c_{ji} = 0.02$ m). c) Effect of the main parameters of the Bouc-Wen model on the shape of the hysteresis loop.

defined as $\mathbf{u}_i = (u_{1,i}, u_{2,i}, \dot{u}_{1,i}, \dot{u}_{2,i}, z_{1,i}, z_{2,i})^{\mathrm{T}}$, so that the equation of motion in generalised coordinates (Eq. (8)) becomes

$$\begin{bmatrix} I_2 & & \\ & \phi_i^T \begin{bmatrix} m_i & \\ & J_i \end{bmatrix} \phi_i & \\ & & I_2 \end{bmatrix} \dot{\mathbf{u}}_i = \begin{pmatrix} \dot{u}_{1,i} \\ \dot{u}_{2,i} \\ -\tilde{F}_{1,i}(u_{1,i}, z_{1,i}) - m_i \ddot{y}_c \\ -\tilde{F}_{2,i}(u_{2,i}, z_{2,i}) - a_i m_i \ddot{y}_c \\ \frac{1}{c_{id}} \psi(\dot{u}_{1i}, z_{1i}) \dot{u}_{1,i} \\ \frac{1}{c_{i\theta}} \psi(\dot{u}_{2i}, z_{2i}) \dot{u}_{2,i} \end{pmatrix} \tag{14}$$

where $i \in \{1, 2\}$ refers to the index of the top and bottom masses of the damper, respectively and I_2 is a 2x2 identity matrix.

Given an imposed clamp motion $y_c(t)$ and considering all parameters with predefined values, this first-order system is then numerically integrated in time-e.g. with the two-stage, one-step SOLVEIVP solver in the SciPy Python package-to obtain the time history

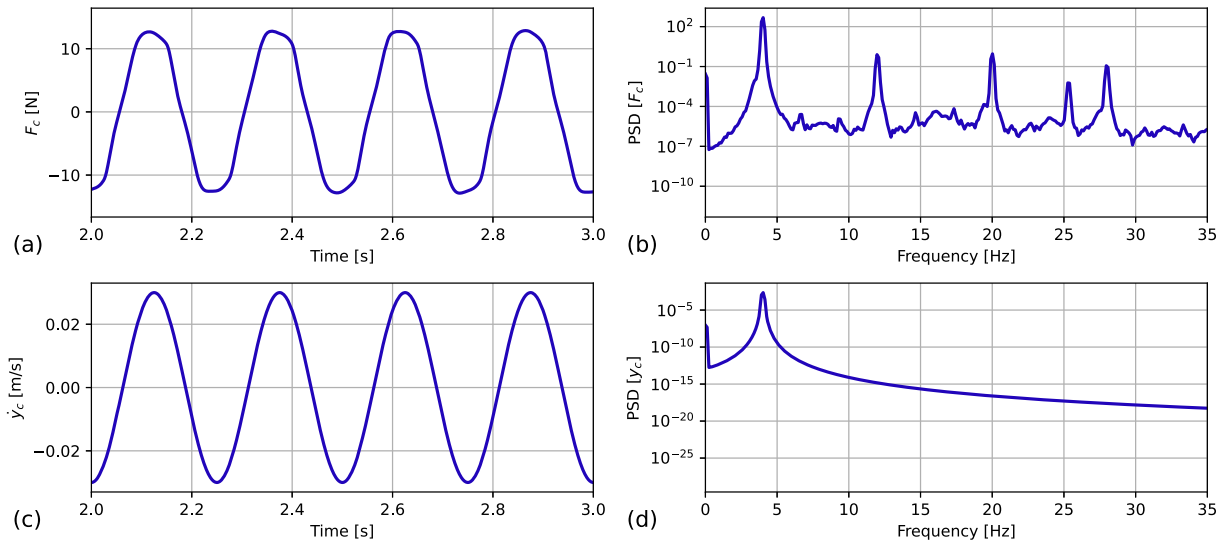

Fig. 5. Portion of (a) output time history and (c) input time history of the analytical model presented in Section 2. On the right of each of the signals, (b) and (d) respectively, is represented their power spectral density.

of the generalised state variables. These can then be transformed back to the physical state variables d_{Gi} and θ_i as shown in Eq. (7). Once the motion of each mass has been determined, the external force at the clamp can be calculated using Eq. (9).

2.3. Numerical example

To better illustrate the behaviour of the model and the influence of its parameters, a simple numerical example is presented. The analysis is structured in three steps. First, the system is subjected to a monoharmonic input signal with fixed amplitude, and the characteristics of the resulting output are analysed in both time and frequency domains. Second, to investigate the model's frequency-dependent behaviour, a sine sweep input with constant amplitude is applied, allowing the response of the system to be observed over a broad frequency range. Finally, the amplitude dependence of the system is explored by feeding sine sweep signals with varying amplitudes into the model. The corresponding variations in the frequency response function are evaluated to highlight the nonlinear nature of the damper and the sensitivity of its dynamic properties to the input amplitude.

The geometry and mass of the damper, as well as the model parameters, used in this example are those measured and identified in the experimental campaign exposed in Section 3 and reported in Tables 1 and 4. A sinusoidal input clamp motion with a frequency of 4 Hz, amplitude $A_{\dot{y}_c} = \max_t \left|\dot{y}_c(t)\right| = 0.03$ m/s, and duration of 30 s is applied to the model. The numerical simulation produces the clamp force $F_c(t)$ as output. To eliminate the initial transients, the time interval 0-2 s is disregarded, and the interval 2-3 s for the input and output time histories is considered. These signals, along with their power spectral densities, are shown in Fig. 5. As shown in the figure, despite the input being a purely monoharmonic sinusoid, the output displays richer frequency content, indicating the model's capability to capture nonlinear dynamic behaviour.

While this example illustrates the model response under a single-frequency excitation, in practice, cable structures exhibit multiple closely spaced vibration modes. Therefore, an effective damper must dissipate energy over a broad frequency range rather than at a single frequency. To characterise the damper's behaviour across this spectrum, it is common in the literature to evaluate its mechanical impedance at the clamp as a function of frequency. To use this function is also the codified way to calculate the power dissipated by this device and therefore measure its efficiency in damping wind-induced vibration [4,10,11]. In a linear configuration, this consists of a scalar input/output function that relates clamp velocity to clamp force. It represents the ground reaction force associated with a specific kinematic input. Assuming a harmonic input motion at the clamp $\dot{y}_c(t) = V_c e^{j\omega t}$ and truncating the Fourier series of the output force at steady state $F_c = F_{c0} e^{j\omega t}$ at the first harmonic, keeping in mind that the system is nonlinear but often behaves semi-linearly for a given vibration amplitude, the impedance function is defined as

$$Z(j\omega) = \frac{F_{c0}(j\omega)}{V_c(j\omega)} \tag{15}$$

To visualise this function, a sine sweep signal can be fed to the system as input clamp velocity $\dot{y}_c(t)$. For example, Fig. 6 shows this kind of input with an amplitude of 0.05 m/s and in the range $0.1 - 50$ Hz. The resulting impedance function calculated with Eq. (15) is shown in Fig. 7. Since, as explained above, the energy dissipation in the messenger cables depends on their deformation, the dynamic response of a Stockbridge damper changes with input amplitude. Therefore, a way to characterise the dynamic behaviour of a Stockbridge damper is to feed input velocity sine sweeps with constant amplitude to visualise the nonlinear behaviour of the device. Fig. 8 shows the impedance function computed numerically for six different values of the clamp input velocity amplitude

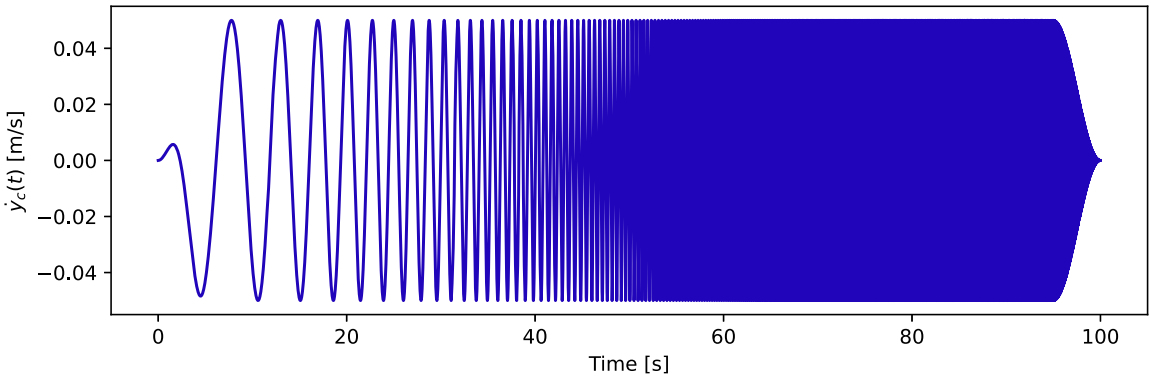

Fig. 6. Time history of a sine sweep velocity input in the range $0.1 - 50\,\text{Hz}$.

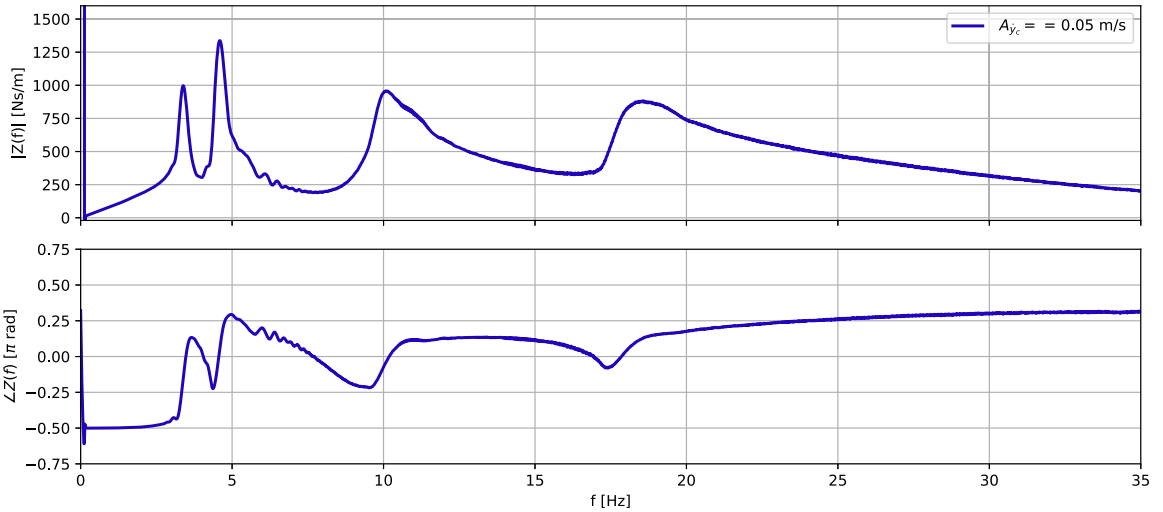

Fig. 7. Absolute value and phase of the numerical impedance function $Z_{\text{num}}(f)$ in function of frequency resulting from a sine sweep clamp velocity input with amplitude $A_{\dot{y}_c} = 0.05\,\text{m/s}$. Numerical values of damper properties are given in Tables 1 and 4.

$A_{\dot{y}_c}$. As can be seen, the proposed model captures this feature, and the modulus of the numerically computed impedance varies as a function of the imposed clamp velocity amplitude.

Fig. 8a shows that the peaks associated with each resonance frequency shift from right to left (i.e., from higher to lower frequencies) as the amplitude of the input motion increases. However, this frequency shift is bounded for each resonance mode between an upper and a lower limiting frequency. Beyond these limits, further increases or decreases in the input amplitude no longer result in lateral movement of the resonance peak, but only in an increase in the peak magnitude. A graphical representation of this behaviour for the generalised coordinate u_{11} is provided in Fig. 9. In this figure, the two asymptotic boundary limits are approximated by black dashed lines. The resonance peaks associated with the generalised coordinate u_{11}, obtained for different input amplitude levels, are highlighted and connected with a red dashed line. The legend provides the amplitude of the generalised coordinate u_{11} for each simulation. This visualisation illustrates how the resonance frequency and maximum amplitude of vibration of the system progressively shift, following a curved path, as the amplitude of the motion increases.

As previously mentioned, the ruling parameters of the model are $k_{ji}^{\min}$, $k_{ji}^{\max}$, and c_{ji} for $i \in \{1,2\}$ and $j \in \{1,2\}$. The stiffness parameters $k_{ji}^{\min}$ and $k_{ji}^{\max}$ determine the location of the two vertical bounds between which the peak of the impedance function shifts, depending on the input amplitude. The frequency of these boundaries can be approximated by

$$f_{ji} = \frac{1}{2\pi}\sqrt{\frac{k_{ji}}{\lambda_{ji}}} \tag{16}$$

where λ_{ji} is one of the diagonal values of the generalised mass matrix of mass i:

$$\mathbf{\Lambda}_i = \boldsymbol{\phi}_i^T \begin{bmatrix} m_i & 0 \\ 0 & \boldsymbol{J}_i \end{bmatrix} \boldsymbol{\phi}, \qquad \lambda_{1i}, \lambda_{2i} = \text{diag}(\mathbf{\Lambda}_i) \tag{17}$$

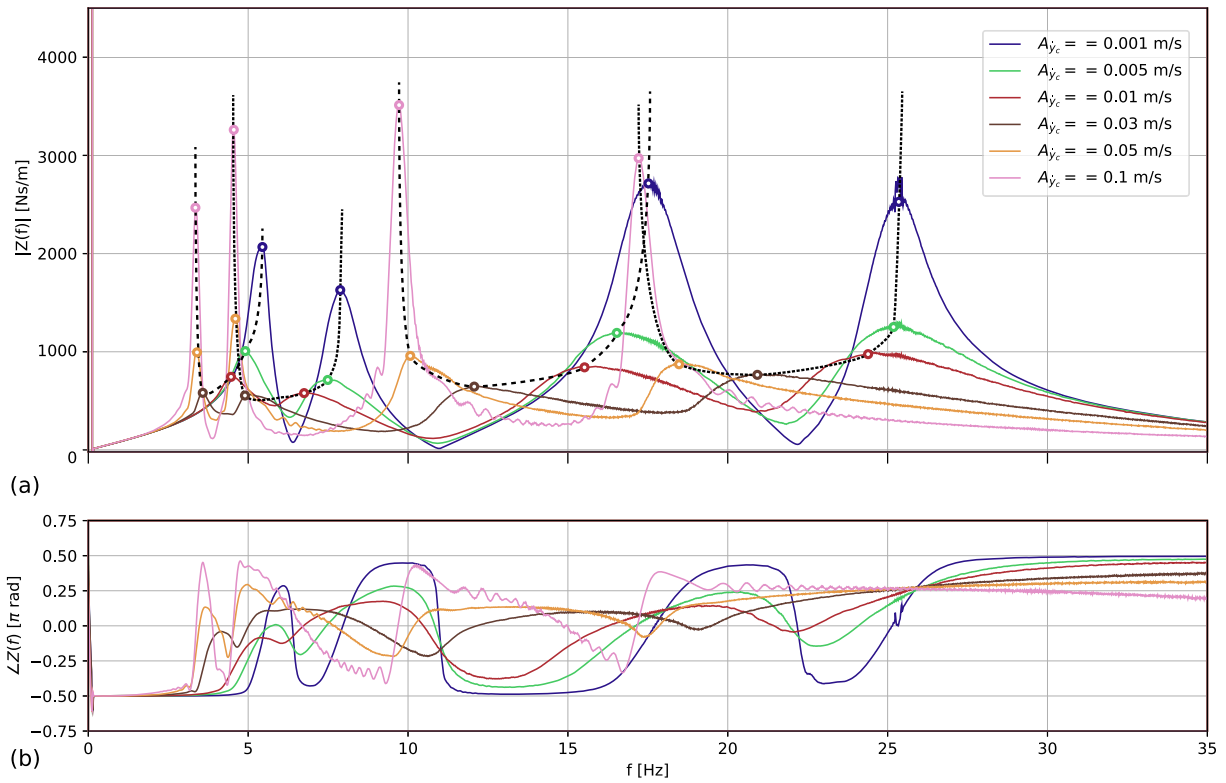

Fig. 8. Absolute value of the numeric impedance function $Z_{\text{num}}(f)$ in function of frequency for an asymmetric Stockbridge damper numerically calculated with the proposed model for six different clamp velocity amplitudes. The black dashed lines indicate the trend of the peaks across the different amplitudes.

Despite some similarity, these limit frequencies are not true natural frequencies as would be defined for a linear system, but define approximate values of the lower or upper bound (respectively using $k_{ji}^{\min}$ or $k_{ji}^{\max}$ in Eq. (16)) of the frequency range inside which the system exhibits the largest dynamic magnification. The parameter c_{ji}, instead, represents the yielding generalised displacement and controls the amplitude range over which the impedance peak transitions between the two bounds. A visual representation of this concept is reported in Fig. 9. Details on how to fine-tune the model parameters from experimental data are given in Section 3.3.

3. Stockbridge damper experimental testing and model parameter tuning

3.1. Experimental setup description

To fit the parameters of the model described in Section 2, a damper from the Hålogaland Bridge was tested in the laboratory of the Structural Engineering Department at NTNU. The damper was excited using a modal vibration shaker (APS 420 ELECTRO-SEIS®, reaction mass 3.8 kg, maximum force 900 N in the range 3 – 20 Hz). A picture (Fig. 10a) and a simplified schematic (Fig. 10b) of the experimental setup are shown in Section 3.1. The shaker rod was connected to a glider equipped with recirculating ball bearings. A C-shaped aluminium bracket incorporating two load cells was mounted on the glider. The damper was attached vertically to the load cells, with the larger mass oriented downward. The shaker was operated in acceleration control mode. As a result, the damper was excited through a prescribed horizontal clamp acceleration, $\ddot{y}_c(t)$, such that the amplitude of the clamp velocity $\dot{y}_c(t)$ would be kept constant. The horizontal clamp force, $F_c(t)$, was measured as the sum of the signals from the two load cells.

To measure the dynamic response of the damper, seven 1-D accelerometers were installed as shown in Fig. 11. Three accelerometers were mounted on each of the two masses. The first accelerometer was positioned at the tip of the messenger cable. Due to spatial constraints and surface roughness, it was not feasible to mount the accelerometer directly on the messenger cable. Therefore, it was instead installed on the outer surface of the masses, with a horizontal offset along the z-axis from the cable tip (accelerometers $A01$ and $A03$ in Fig. 11b). Since the mass is rigid, the motion of the centre of mass ($d_{Gi}(t)$) can be derived by transforming measurements in other locations. Therefore, the actual acceleration $\ddot{d}_{Gi}(t)$ was derived with the following equaiton:

$$\ddot{d}_{Gi} = \ddot{u}_{xi} - \frac{L_{iz}}{2}\ddot{\alpha}_i + \eta_i e_{Gi}\ddot{\theta}_i \tag{18}$$

where $\ddot{u}_{xi}$ is the x axis acceleration from the sensor $A01$, if $i = 1$, or $A03$, if $i = 2$, and $\ddot{\alpha}_i$ is the angular acceleration around the y axis of mass i. To be able to capture the rotation of each mass around the z-axis, a second accelerometer was placed as far as possible

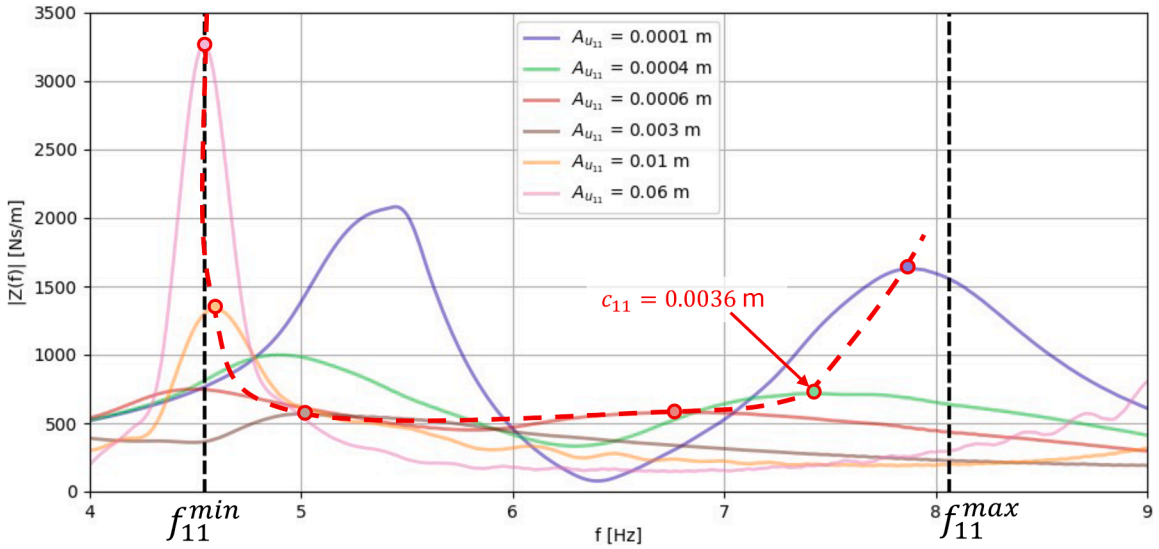

Fig. 9. Illustration of the transition of resonance frequency with amplitude of input and existence of upper and lower bounds corresponding to the frequencies obtained with stiffnesses $k^{\min}$ and $k^{\max}$. The legend provides the amplitude of the generalised coordinate u_{11} for each simulation. The red arrow indicates which amplitude of the generalised displacement u_{11} to use to have an estimate of the parameter c_{11}. (For interpretation of the references to colour in this figure legend, the reader is referred to the web version of this article.)

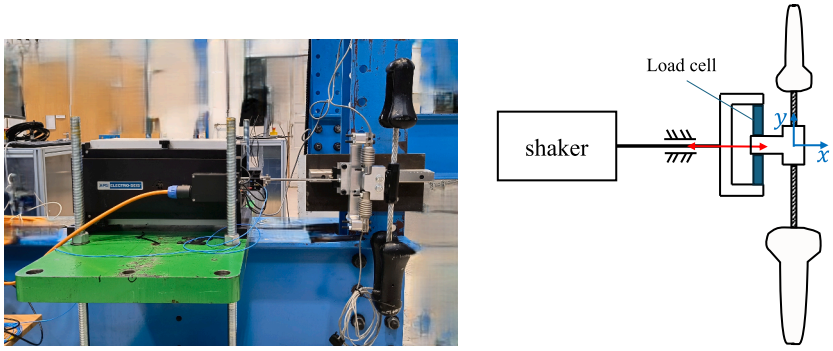

(a) (b)

Fig. 10. a) Picture of the experimental setup for the asymmetric Stockbridge damper from the Hålogaland bridge. b) Simplified scheme of the experimental setup.

from the centroid in the x-y plane (accelerometers $A02$ and $A04$ in Fig. 11b). To capture the rotation around the y axis, a third accelerometer was placed symmetrically to the first one with respect to the x-y plane (accelerometers $A06$ and $A07$ in Fig. 11b). An additional accelerometer was mounted on the clamp (accelerometer $A05$ in Fig. 11b), which directly measures the first derivative of the input clamp velocity $\dot{y}_c(t)$. The rotations around the z-axis, θ_i, and the y-axis, α_i, were computed from the measured accelerations as

$$\ddot{\theta}_1 = \frac{\ddot{u}_{A02} - \ddot{u}_{A01}}{L_{1y}}, \quad \ddot{\alpha}_1 = \frac{\ddot{u}_{A01} - \ddot{u}_{A06}}{L_{1z}} \tag{19a}$$

$$\ddot{\theta}_2 = \frac{\ddot{u}_{A03} - \ddot{u}_{A04}}{L_{2y}}, \quad \ddot{\alpha}_2 = \frac{\ddot{u}_{A03} - \ddot{u}_{A07}}{L_{2z}} \tag{19b}$$

The distances between the accelerometers are reported in Table 2.

3.2. Analysis of experimental data

Before analysing the results of the sine sweep tests, it is useful to illustrate the two fundamental deformation shapes exhibited by each half of the damper. Fig. 12 shows a portion of the recorded signal from the two accelerometers $A01$ and $A02$ (see Fig. 11b) positioned, respectively, above and below the centre of mass. Fig. 12a shows, at approximately 5 Hz, the mass vibrating in its first mode, dominated by lateral translation. In this case, the two accelerometers move in phase, with $A01$ showing a slightly larger

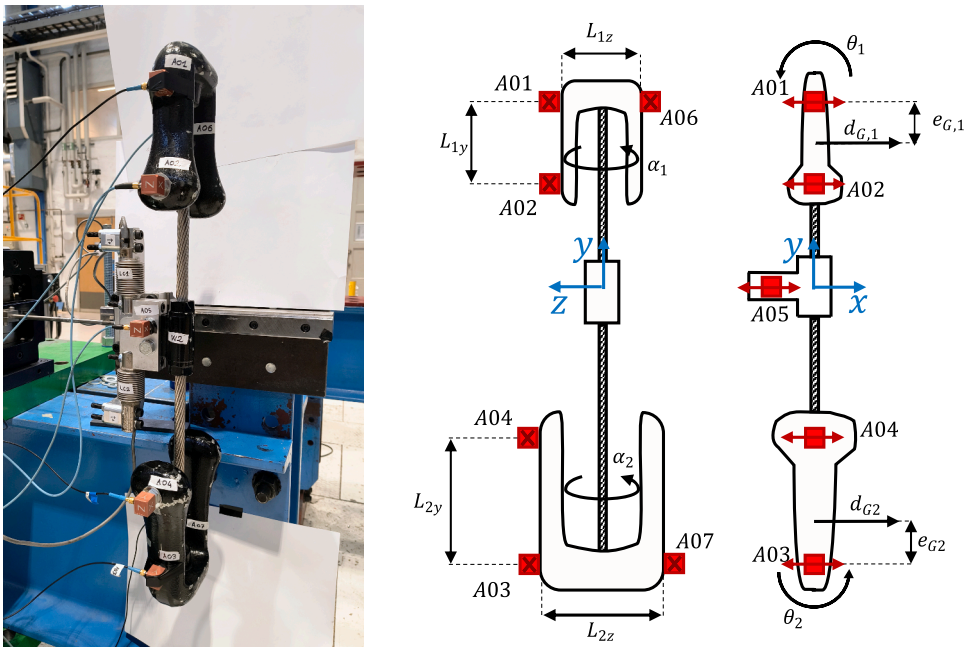

(a) (b)

Fig. 11. a) Picture of the instrumented damper. b) Scheme of the instrumented damper with lateral (left) and frontal (right) views. In red are marked the locations of the accelerometers. (For interpretation of the references to colour in this figure legend, the reader is referred to the web version of this article.)

Table 2
Distances between accelerometers used to compute rotational accelerations, as illustrated in Fig. 11.

Parameter	Value [m]
L_{1y}	0.104
L_{1z}	0.106
L_{2y}	0.127
L_{2z}	0.118

amplitude because it is located further from the clamp. In Fig. 12b is shown the mass vibrating in the second mode, at around 21 Hz, which is primarily rotational. The corresponding time histories reveal the two accelerometers oscillating in opposite phase: since $A01$ and $A02$ are positioned symmetrically with respect to the centroid, their readings reflect the rotational motion. Moreover, because the centroid is closer to $A01$, the outer accelerometer $A02$ registers the larger response amplitude. These observations confirm, from an experimental perspective, that the messenger cable behaves as expected, exhibiting two dominant deformation patterns resembling those of a cantilever beam with an end mass.

The damper has been excited with logarithmic sine sweeps with target clamp velocity amplitude $A_{\dot{y}_c}$ that is constant for each test. Different amplitudes have been tested to highlight the nonlinear behaviour of the device. Standards in the field of overhead power lines [3,4] suggest a constant velocity amplitude of 0.1 m/s to characterise this kind of device. However, there is no such standard for bridge hanger applications. Therefore, the range of clamp velocity amplitudes for the present work was selected based on the velocity amplitudes observed in the field [2]. A more detailed discussion of the selected test amplitudes and additional results at $A_{\dot{y}_c} = 0.1$ m/s is provided in A.

Figs. 13 and 14 show, as an example, the measured time histories of the clamp velocity and clamp force, respectively, for two of the tested clamp velocity amplitudes. It is interesting to notice that a change of only 0.01 m/s in the input amplitude in Fig. 13, causes noticeable shifts in both the height and frequency of the resonance peaks in the force signal in Fig. 14. This confirms the nonlinear behaviour of the device under investigation. From the time history of the clamp force $F_c(t)$, shown in Fig. 14, it is evident that, for both tested amplitudes, the frequency sweep excites the four resonances of the damper. Each resonance is reflected as a distinct peak in the measured force response, corresponding to the dynamic amplification associated with the device's resonances.

Due to limitations in the shaker's capability to exactly reproduce the prescribed motion, the clamp velocity amplitude exhibited slight variations. It was not strictly constant nor harmonic throughout the excitation, particularly near resonance frequencies, due to the large inertial forces. These fluctuations are evident in the clamp velocity traces shown in Fig. 13. Another limitation in the excitation system can be observed in Fig. 15. As shown in Fig. 15a, at low frequencies the shaker struggles to generate a perfectly

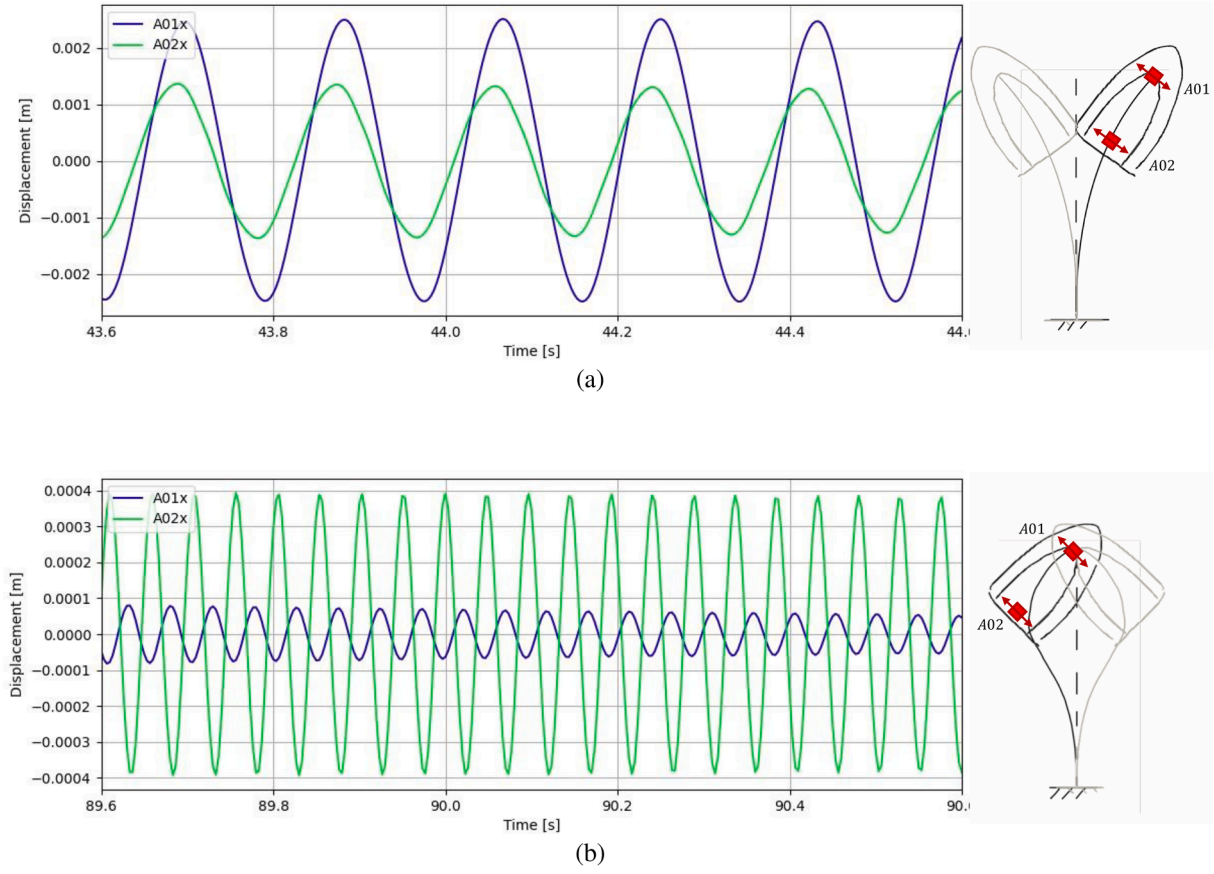

Fig. 12. Time histories of the integrated measurements from sensors $A01$ and $A02$ at (a) 5.2 Hz and (b) 21 Hz. The excitation is a sine sweep with amplitude $A_{\ddot{y}_c} = 0.03\,\mathrm{m/s^2}$. On the right, the corresponding deformation shapes are shown schematically, exagerating the amplitude of displacements.

sinusoidal motion, producing a more pointed, non-sinusoidal periodic waveform instead. The presence of this distortion is further confirmed by the spectrogram in Fig. 13, where the input signal exhibits a multiharmonic content: additional weaker frequency components appear as distinct bands at integer multiples of the instantaneous sweep frequency. However, as the frequency increases, the excitation gradually recovers a clean sinusoidal shape, as illustrated in Fig. 15b, since the integer multiples of the target frequency become more widely spaced and their relative influence on the waveform diminishes.

Using these time histories and Eq. (15), the impedance of the damper was computed in the frequency domain for each of the five tests with different velocity amplitudes, obtaining the curves shown in Fig. 16. This plot demonstrates how the experimental impedance of the damper changes with the input amplitude. In particular, as the amplitude of the imposed motion increases, the damper becomes softer on average, and the four resonance peaks of the transfer function shift toward lower frequencies, a feature that the presented model is precisely able to emulate. By extracting the peak values of the absolute value of the impedance from Fig. 16a, the trends shown in Fig. 17 were obtained. The coordinates of the peaks generating the trend in Fig. 17 are also reported in Table 3. These trends reveal that the peaks' position and amplitude of each vibration mode follow a curved, amplitude-dependent path. This behaviour differs for each resonance and represents the experimental realisation of the trends illustrated numerically in Section 2.3. In Fig. 17, it can be seen how the trajectories are bounded by lower and upper frequency limits which correspond to the pre-yield stiffness $k_{\max}$ and the post-yielding stiffness $k_{\min}$ of each of the messenger cables. This concept was already illustrated in the numerical example of Fig. 9, where the boundaries of the peak trajectories were shown schematically. Identifying these boundaries, together with estimating the transition amplitude c_{ji} for each degree of freedom, is essential for accurately calibrating the proposed Bouc-Wen model.

3.3. Tuning of model parameters

The parameters of the numerical model of the asymmetric Stockbridge damper, introduced in Section 2.2, were calibrated using the experimental data presented in Section 3.2. In particular, the trajectories of the experimental resonance impedance peaks shown in Fig. 17, and reported in Table 3, served as the primary reference for tuning the model parameters.

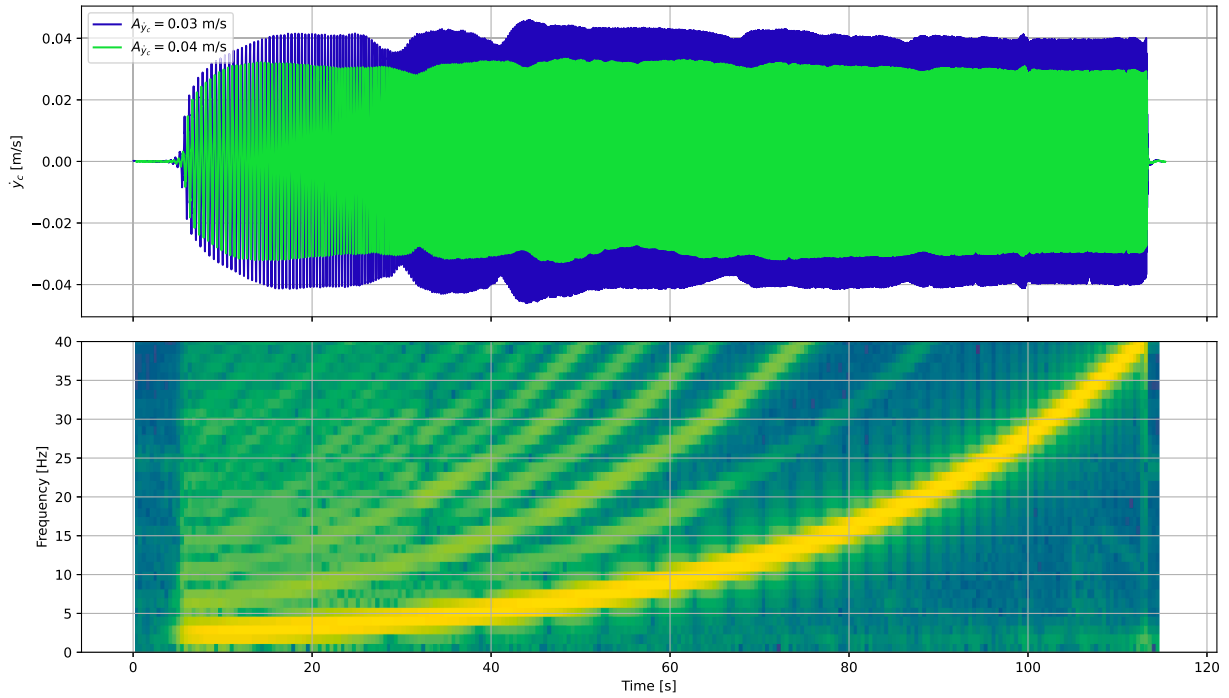

Fig. 13. Experimental sine sweep of the input clamp velocity used to characterise the dynamic response of the Stockbridge damper. Example of two clamp velocity amplitudes. Time history above and spectrogram of the 0.04 m/s time history below.

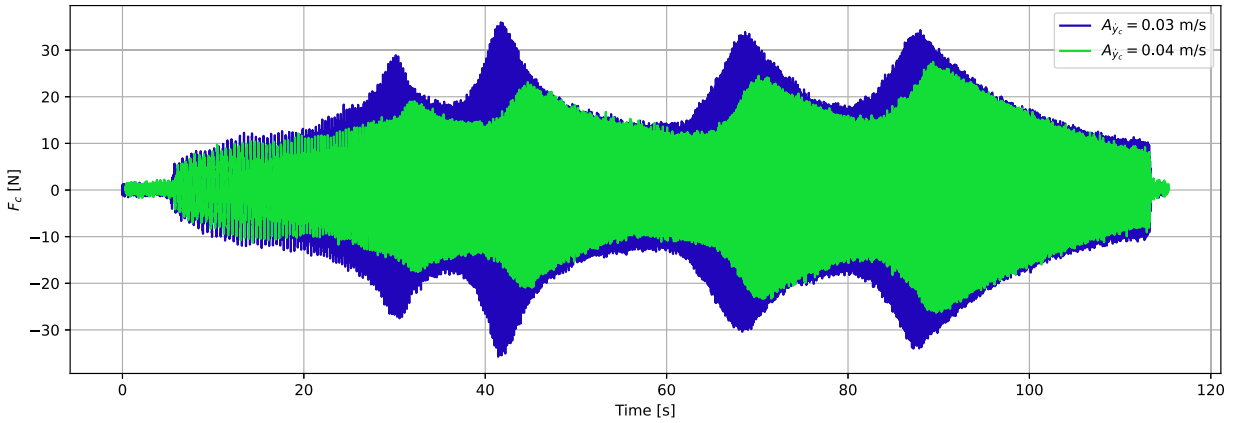

Fig. 14. Experimental output clamp force resulting from the input clamp velocity shown in Fig. 13.

Table 3
Variation of the position in [Hz] of the peaks of the absolute value of the experimental impedance function ($|Z_{\text{exp}}(f)|$) with the amplitude of the clamp velocity $A_{\dot{y}_c(t)}$, for the tested asymmetric Stockbridge damper. These values are plotted in Fig. 17.

$A_{\dot{y}_c(t)}$ [m/s]	0.01	0.02	0.03	0.04	0.05
1st mode ([Hz], [Ns/m])					
Translation bottom mass ($d_{G,2}$) 2nd mode ([Hz], [Ns/m])	(5.13, 839.87)	(4.10, 680.12)	(3.74, 593.98)	(3.52, 734.21)	(3.44, 1158.52)
Translation top mass ($d_{G,1}$) 3rd mode ([Hz], [Ns/m])	(8.20, 856.22)	(6.23, 641.10)	(5.35, 642.52)	(4.98, 896.28)	(4.76, 1410.15)
Rotation bottom mass (θ_2) 4th mode ([Hz], [Ns/m])	(16.04, 951.93)	(13.18, 798.74)	(11.43, 772.21)	(10.69, 819.06)	(10.18, 1046.51)
Rotation top mass (θ_1)	(26.22, 1307.59)	(22.41, 959.31)	(20.00, 845.98)	(18.97, 822.00)	(17.87, 1006.81)

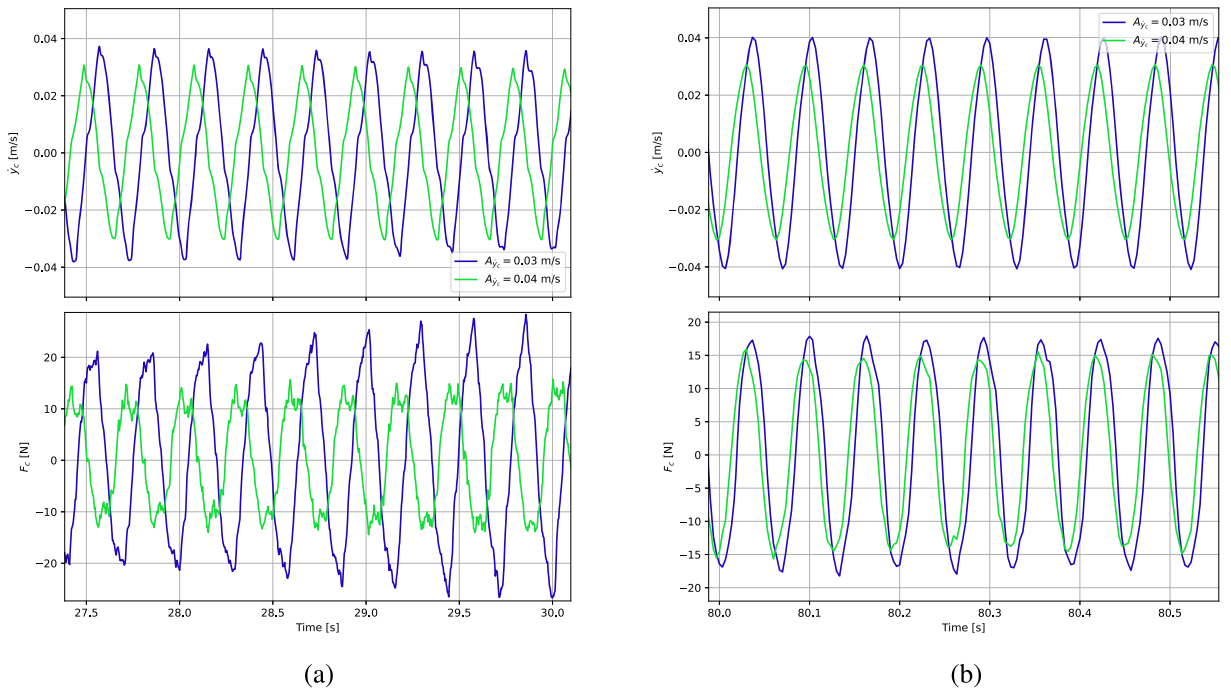

Fig. 15. a) Zoom on the first part of the sweep input-output time history, corresponding to low frequencies (below 5 Hz). b) Zoom on the second part of the sweep input-output time history, corresponding to high frequencies (15 – 20 Hz).

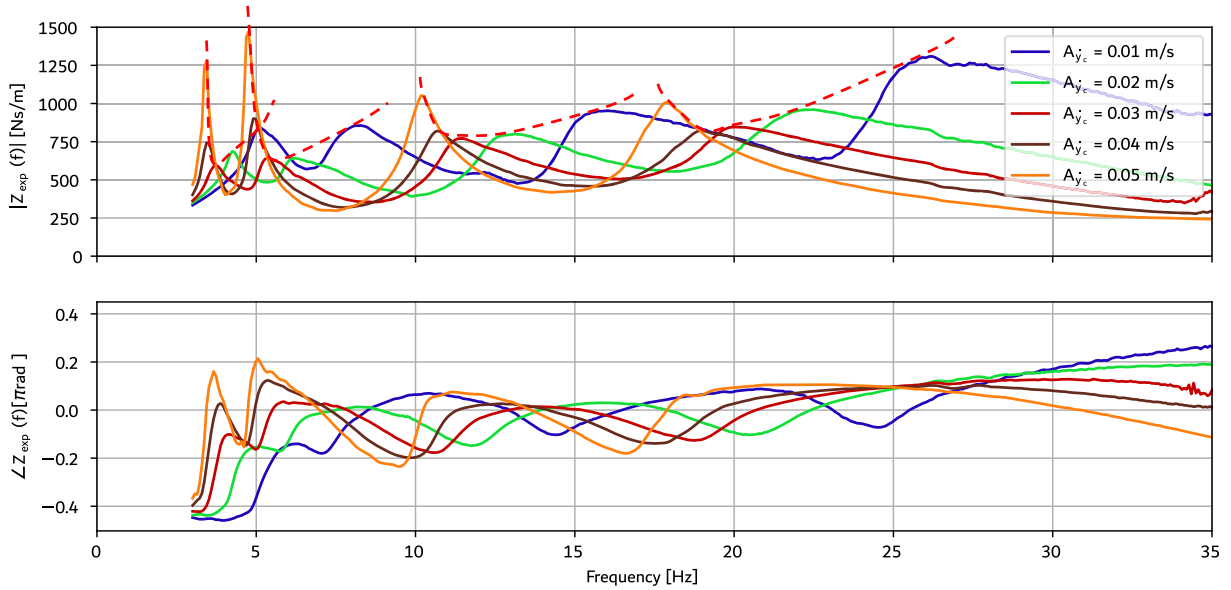

Fig. 16. Modulus and phase of the experimental impedance function $Z_{\text{exp}}(f)$ for five different amplitudes of the input clamp velocity. The red dashed lines indicate the trend of the peaks across the different amplitudes. (For interpretation of the references to colour in this figure legend, the reader is referred to the web version of this article.)

Firstly, the scaling parameters a_i and b_i were identified for each mass as the ratio between the amplitude of the centre of mass displacement $A_{d_{Gi}}$ and rotation A_{θ_i} at the resonance peaks given a clamp velocity amplitude. This was used as an initial guess, then the values of the parameters were adjusted to improve the fitting with the experimental impedance peaks; the final values are reported in Table 4. Thanks to the generalised coordinates transformation described in Section 2.1, each of the four peak trends could be analysed separately. This allowed each of the four Bouc-Wen models, corresponding to the four uncoupled degrees of freedom of the damper model, to be tuned independently. Consequently, only three parameters needed to be identified at a time, which made the training

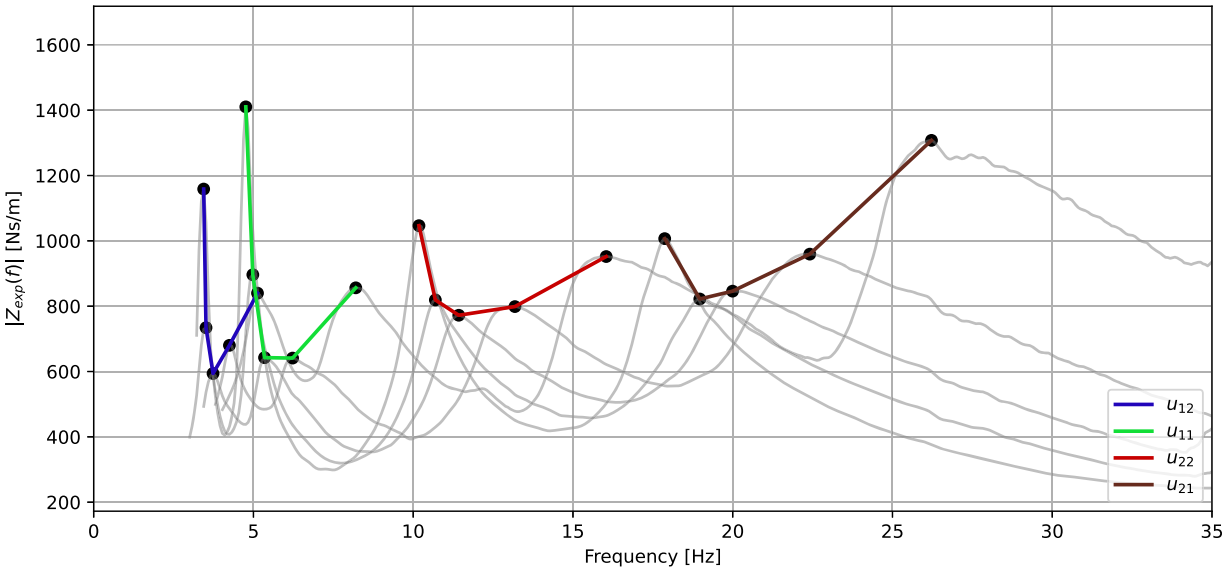

Fig. 17. Trajectories of the experimental resonance peaks in the (frequency, impedance) space, for several clamp velocity amplitudes $A_{\dot{y}_c} = [0.01, 0.02, 0.03, 0.05]$ m/s for each degree of freedom.

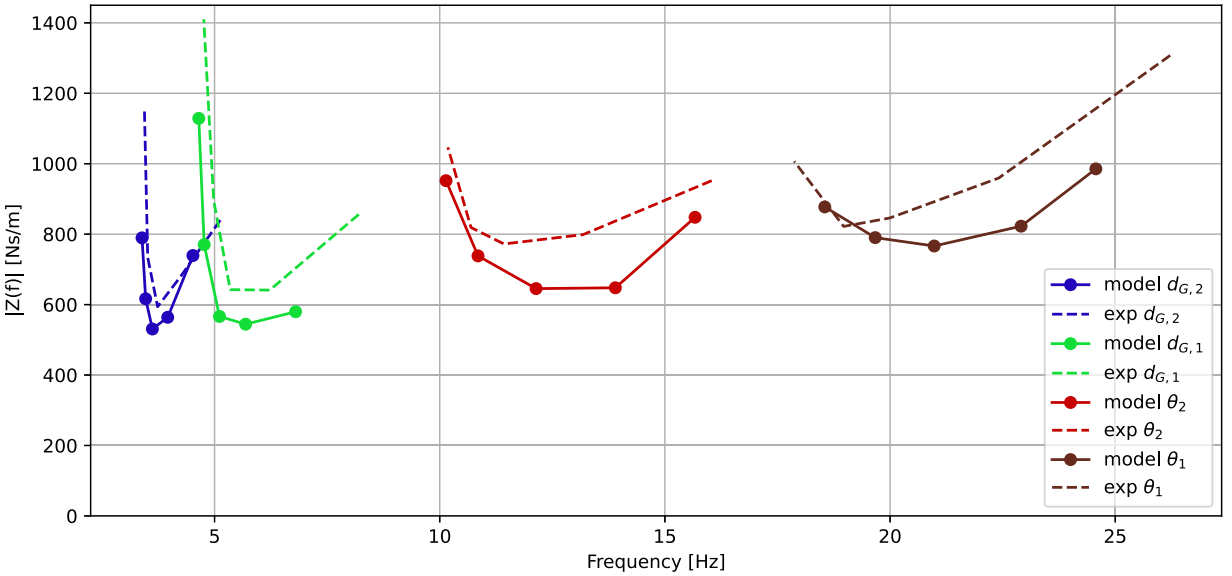

Fig. 18. Trajectories of the four peaks of the modulus of the impedance function of the Stockbridge damper. The dashed line represents the experimental data, while the continuous line represents the tuned numerical Bouc-Wen model.

possible by simple hand adjustment. The initial estimates for the stiffness parameters $k_{ji}^{\min}$, $k_{ji}^{\max}$ were obtained by inverting Eq. (16). A practical approach for selecting an initial estimate for c_{ji} involves analysing the impedance function at varying input amplitudes. As previously discussed, each resonance peak follows a curved trajectory as the input amplitude increases. To estimate c_{ji}, one should observe the amplitude of the generalised coordinate (j, i) at an input level where the corresponding impedance peak has begun to deviate from its upper frequency bound and lies in the lower portion of this path. At that point, the observed amplitude of the generalised coordinate $A_{u_{ji}}$ provides a suitable order of magnitude for the corresponding c_{ji} value. Refer to Fig. 9 for a visualisation of this concept. It should be emphasised that these procedures, and in particular the approach used for c_{ji}, only provide first-guess values of the parameters, which then serve as starting points for the iterative tuning process.

Once an initial guess for the parameters was obtained, the peak trends of the numerical impedance function $Z_{\text{num}}(f)$ (solid lines in Figs. 18 and 19) were iteratively adjusted using a trial-and-error approach to match the experimental trends (dashed lines in the same figures). In practice, this was carried out by numerically simulating the system response to the five sine sweep inputs, each corresponding to one of the amplitudes used in the experimental tests. For each case, the impedance function was computed from the

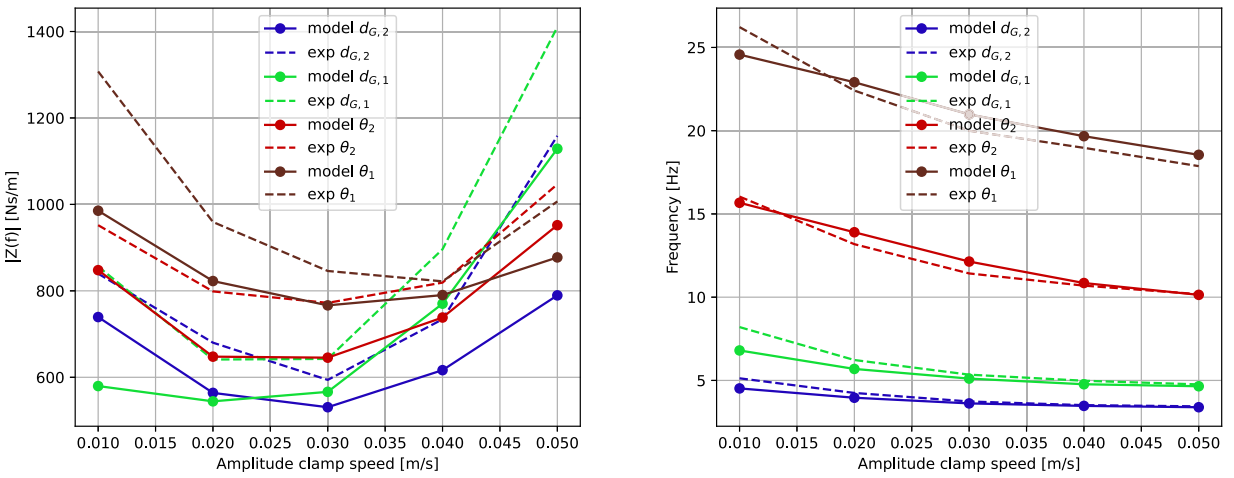

Fig. 19. Comparison between the peaks of the damper's impedance function measured experimentally (dashed) and computed numerically (solid line). a) Comparison of the peaks' height for the four degrees of freedom for different input amplitudes. b) Comparison of the peaks' frequency for the four degrees of freedom for different input amplitudes.

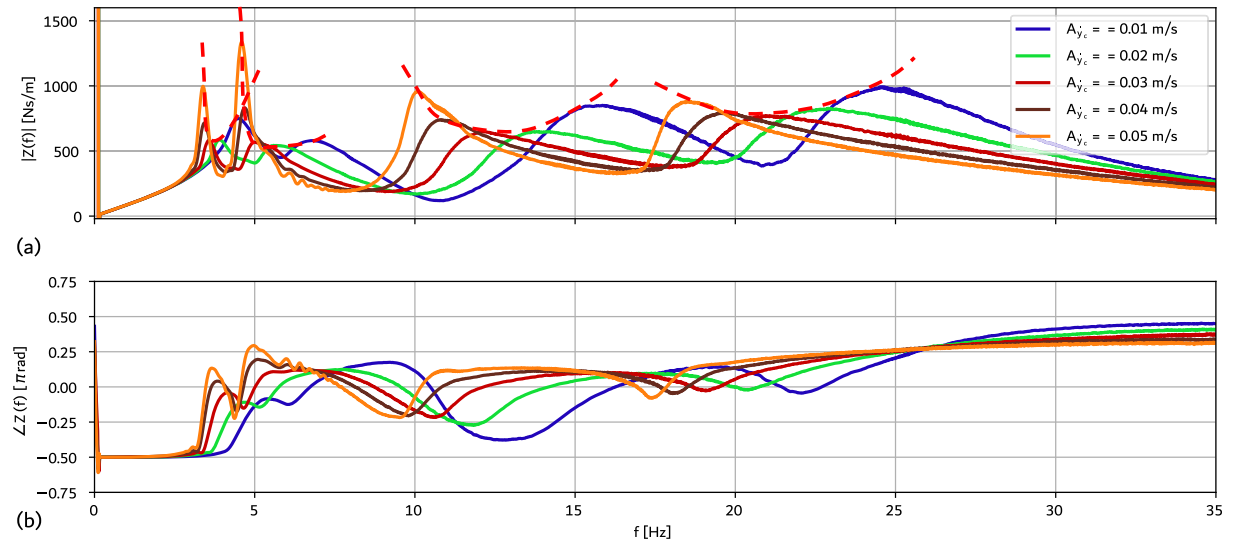

Fig. 20. Modulus and phase of the numerical impedance function $Z_{num}(f)$ for five different amplitudes of the input clamp velocity and parameter values shown in Table 4. The red dashed lines indicate the trend of the peaks across the different amplitudes. (For interpretation of the references to colour in this figure legend, the reader is referred to the web version of this article.)

simulated response using Eq. (15), and the resonance peak positions were extracted. These trajectories in the numerical simulations were then compared with the experimental ones-both globally, on the amplitude-frequency plane as shown in Fig. 18, and separately for amplitude and frequency values at each input level, as shown in Fig. 19a and b. Based on these comparisons, the parameters were iteratively adjusted to improve the fit, and the process was repeated until satisfactory agreement was achieved.

The final parameter set, calibrated on experimental data, is summarised in Table 4. The corresponding numerical impedance functions computed at the last iteration are shown in Fig. 20, which serves as the numerical counterpart of the experimental results presented in Fig. 16.

3.4. Evaluation of the model performance - Multiharmonic excitation

To validate the trained model, a time history recorded in the field was used as excitation to the shaker. The recording came from the permanent monitoring system on the Hålogaland Bridge in Norway. For a detailed description of the monitoring system, refer

Table 4
Model parameters for the four degrees of freedom Bouc-Wen model tuned on experimental data of an asymmetric Stockbridge damper nominally identical to the ones installed on the Hålogaland suspension bridge [2].

	Top mass translation	Top mass rotation	Bottom mass translation	Bottom mass rotation
	$i = 1$ $j = 1$	$i = 1$ $j = 2$	$i = 2$ $j = 1$	$i = 2$ $j = 2$
$k_{ji}^{\min}$	4,600	230	4,800	140
$k_{ji}^{\max}$	14,500	500	12,700	480
c_{ji}	0.00036	0.0025	0.00055	0.0021
n	1	1	1	1
σ	1	1	1	1
a_i	0.01	–	–0.001	–
b_i	–	–7		7

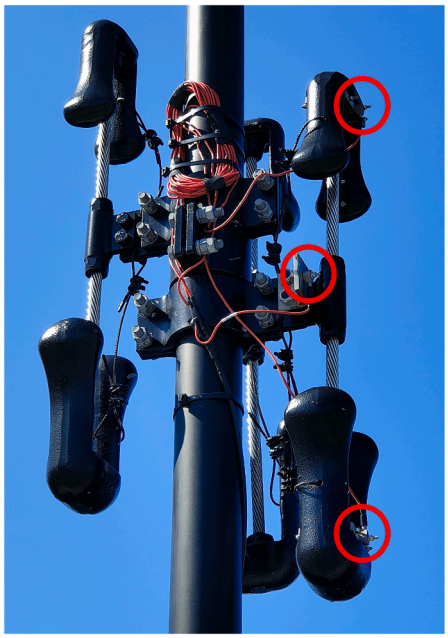

Fig. 21. Three Stockbridge dampers on a hanger of the Hålogaland bridge in Narvik, Norway. On the right-most damper, three accelerometers have been mounted. They are marked with red circles in the figure. (For interpretation of the references to colour in this figure legend, the reader is referred to the web version of this article.)

to [2,37]. As part of the monitoring project, one of the dampers installed on the hangers was instrumented with three mono-axial accelerometers as shown in Fig. 21.

One time history from the accelerometer on the clamp was selected to validate the model. This specific time series was selected since it has its main frequency content in the $0 - 30$ Hz range. The time history recorded in the field, to be played on the APS 420 shaker, was first upsampled from 128 Hz to 2000 Hz, then low-pass filtered at 45 Hz and finally tapered at the start and at the end with an exponential window. The processed time series was integrated in time to obtain the velocity signal, which was used as input to the numerical model. The final input signal is shown in Fig. 22. In addition to the full time history (a), the figure also shows a zoomed portion (b), where it is clear that the velocity is not a narrowband process. The signal's power spectral density is also shown in Fig. 22c. The acceleration signal was applied as input to the damper in the laboratory setup presented in Section 3.1, where the output force and internal dynamic response were recorded. The velocity signal was fed into the numerical model to validate its performance against the experimental results.

The comparison between experimental and numerical results is shown in Fig. 23, which displays both time-domain and frequency-domain representations. The input signal contains energy in the 0-5 Hz and 10-20 Hz bands, activating simultaneously all four resonance modes of the damper. This contrasts with the training phase, where each mode was identified independently using monoharmonic sine sweeps, highlighting the model's ability to generalise its behaviour under multiharmonic excitation. The model performs well in predicting the lateral degrees of freedom (d_{G1}, d_{G2}) and the output force F_c in the entire frequency range. The rotational motions (θ_1, θ_2) are also accurately reconstructed across the excited frequency content. Prediction accuracy diminishes above 30 Hz due to limited input energy in that range.

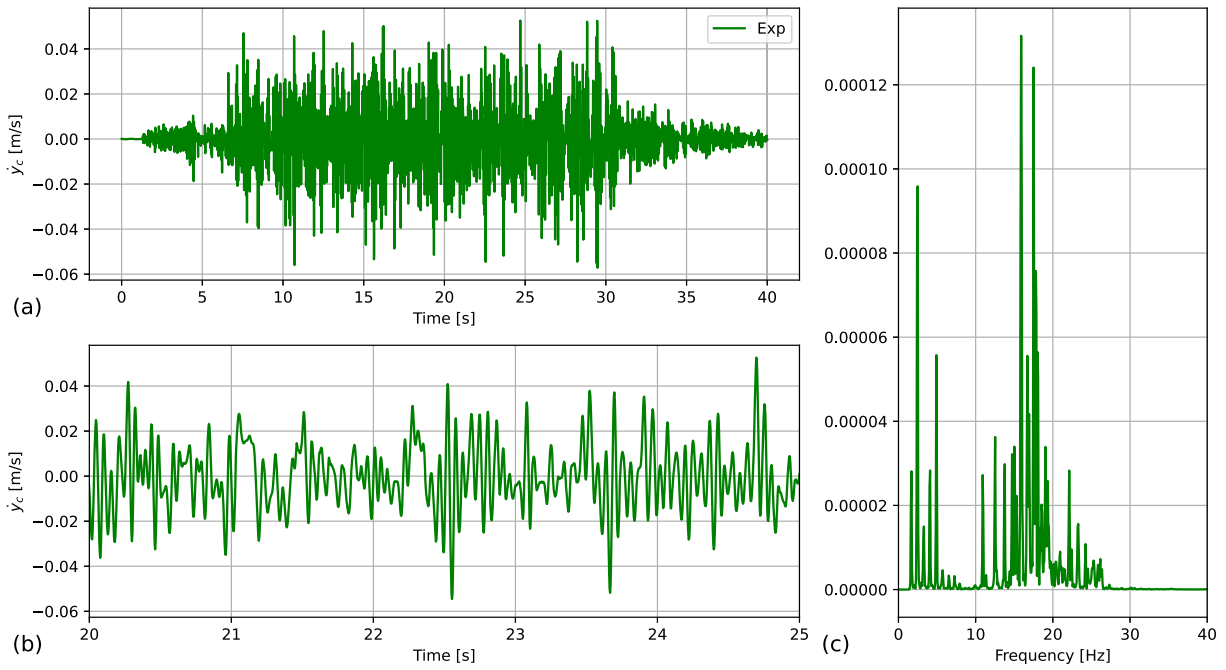

Fig. 22. Time and frequency representation of the processed field-recorded input that was reproduced with the shaker.

While the full nonlinear simulation provides a detailed prediction of both internal and external responses, it is important to benchmark it against the traditional approach commonly used in engineering practice. In typical applications, once a Stockbridge damper is tested, its impedance function is identified experimentally at a fixed velocity amplitude and used as a linear transfer function. Next, the output response is calculated in a simplified manner. When the damper is subjected to multiharmonic excitation, given the input velocity spectrum $S_{\dot{y}_c\dot{y}_c}(f)$, the output force spectrum $S_{F_cF_c}(f)$ is obtained as

$$S_{F_cF_c}(f) = \left|Z(f;A_{\dot{y}_c})\right|^2 S_{\dot{y}_c\dot{y}_c}(f), \tag{20}$$

where $Z(f;A_{\dot{y}_c})$ is the experimentally measured impedance at the chosen input velocity amplitude $A_{\dot{y}_c}$. This simplified, frequency-domain approach assumes linear superposition and neglects any amplitude-dependent effects or nonlinear internal dynamics. It yields an estimate of the output force spectrum without carrying out any nonlinear simulation and forms the conventional basis for assessing damper performance. This approach is limited by the fact that a representative input amplitude $A_{\dot{y}_c}$ must be prescribed in advance. In the literature on Stockbridge dampers for overhead transmission lines, typical values of $A_{\dot{y}_c}$ used for impedance identification are 1-2 m/s, as codified in standard testing procedures [4]. Given the time series shown in Fig. 22, the input amplitude was assumed here in the range 0.01-0.05 m/s.

Fig. 24 shows a comparison between the full nonlinear simulation and the impedance-based approach for the reconstruction of the power spectral density of the clamp force F_c for the case analysed here. The shaded region reflects the variation in predicted output spectral density, for this specific case, obtained by evaluating the impedance at fixed amplitudes between 0.01 and 0.05 m/s, highlighting the sensitivity of this method to the chosen amplitude. For example, we can observe variability in the height of the peaks in the $2-5$ Hz range. Referring back to Fig. 18, it can be seen that in this region the peak heights are strongly amplitude-dependent: the response magnification at $A_{\dot{y}_c} = 0.05$ m/s is almost twice as large as that at $A_{\dot{y}_c} = 0.01$ m/s. At the same time, the corresponding peak trajectories exhibit a relatively narrow V-shape, indicating limited frequency variation. This combination explains why the shaded region in Fig. 24 shows high uncertainty in peak height but comparatively little shift in frequency in this region. The opposite trend is observed in the 25-30 Hz range, where the positions of the peaks in the impedance function vary significantly with $A_{\dot{y}_c}$, proportionally more than their height, see Fig. 18. As a result, the shaded region in Fig. 24 primarily reflects uncertainty in peak location rather than in peak magnitude.

To quantitatively compare the two output power spectral densities, the Wasserstein distance is introduced as a performance metric. The Wasserstein distance, also known as the Earth Mover's Distance or Kantorovich-Rubinstein metric, quantifies the minimal effort required to transform one probability distribution into another by optimally transporting probability mass [38,39].

$$W(P,Q) = \inf_{\gamma\in\Gamma(P,Q)} \int_{\mathbb{R}\times\mathbb{R}} |x-y|\, d\gamma(x,y) \tag{21}$$

In Eq. (21), $\Gamma(P,Q)$ denotes the set of all joint distributions $\gamma(x,y)$ with marginals P and Q, and $|x-y|$ represents the ground distance (here, in frequency units). The integral quantifies the total "effort" required to morph P into Q, making this metric particularly suitable for comparing spectral distributions with similar energy content but non-perfectly aligned peaks. To make this metric meaningful,

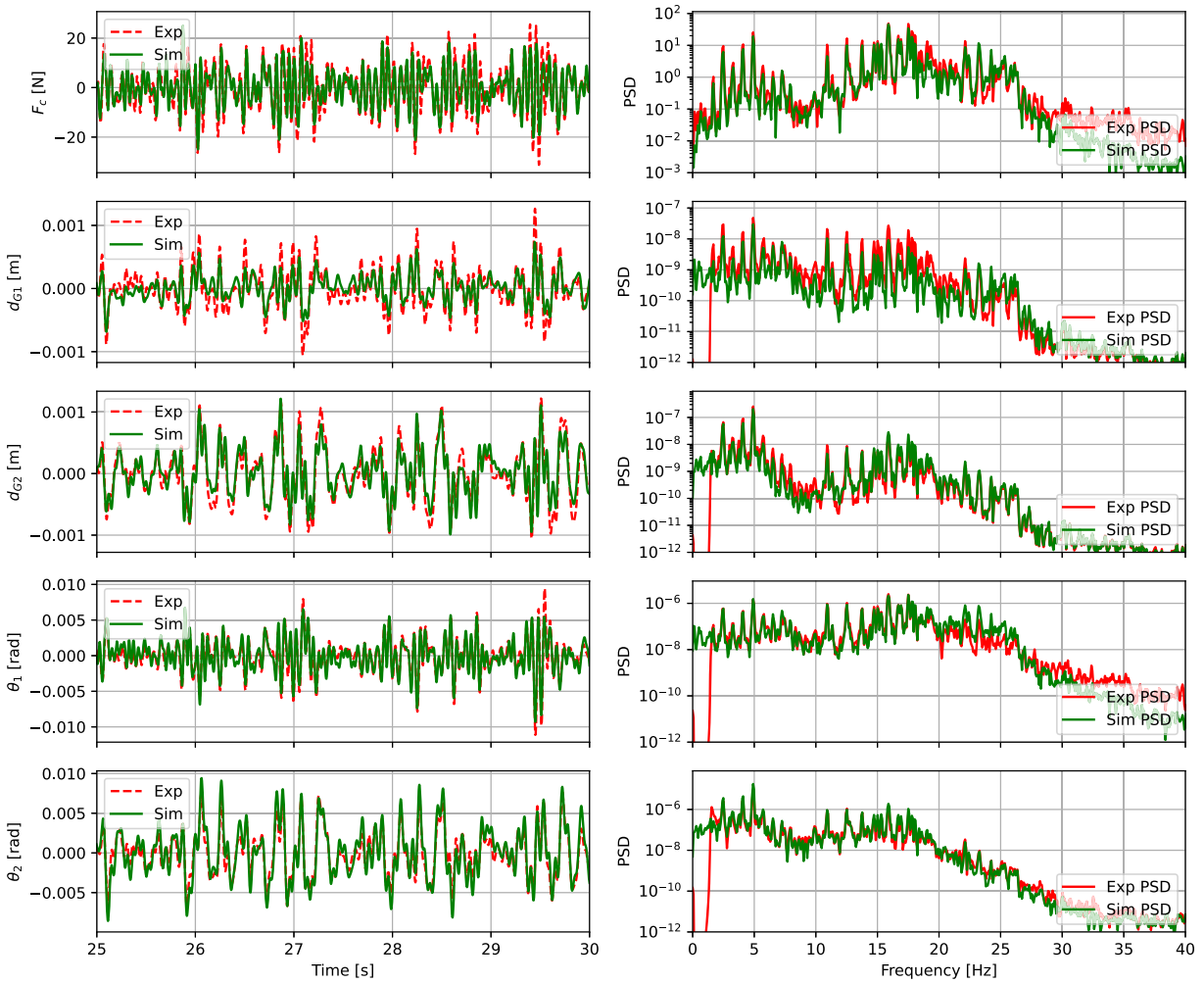

Fig. 23. Output of the presented numerical model given the input shown in Fig. 22. The internal dynamics and output force are shown in both time and frequency domains.

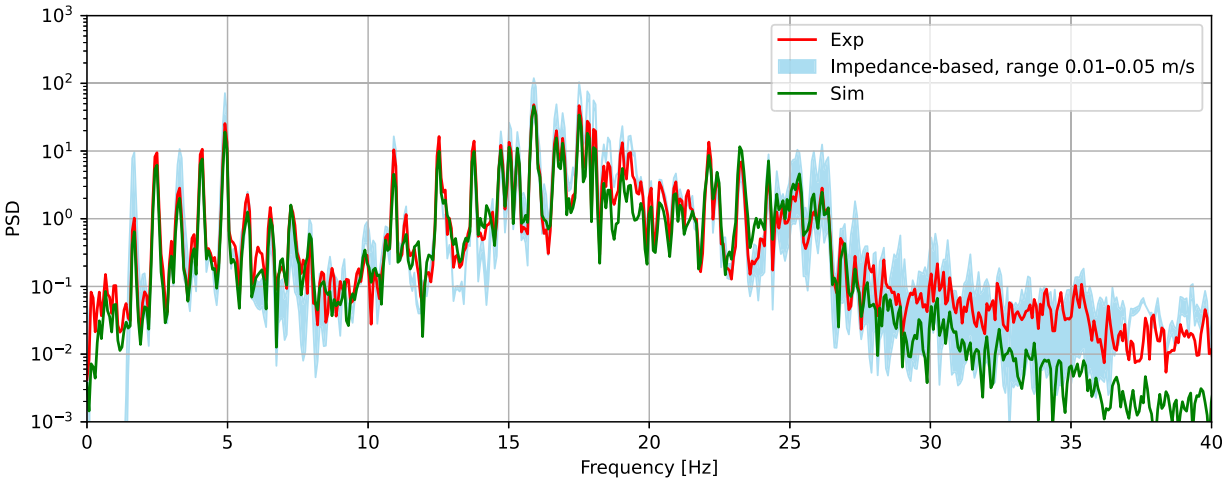

Fig. 24. Power spectral density of the clamp force F_c (top right in Fig. 23) reconstructed with the impedance-based method for a range of input amplitudes (light-blue shaded region) and with the full numerical simulation (green continuous line). (For interpretation of the references to colour in this figure legend, the reader is referred to the web version of this article.)

Table 5
Wasserstein distances computed for the power spectral density of the output force between the experimental data and the two numerical methods, under three different frequency bands.

Frequency range of evaluation for W-index	2–15 Hz	15–25 Hz	25–40 Hz
W-Index Exp - Sim (Nonlin Bouc-Wen)	0.276	0.423	1.126
W-Index Exp - Impedance-based with $A_{\dot{y}_c} = 0.01$m/s	2.004	0.699	0.813
W-Index Exp - Impedance-based with $A_{\dot{y}_c} = 0.04$m/s	0.909	0.458	0.508

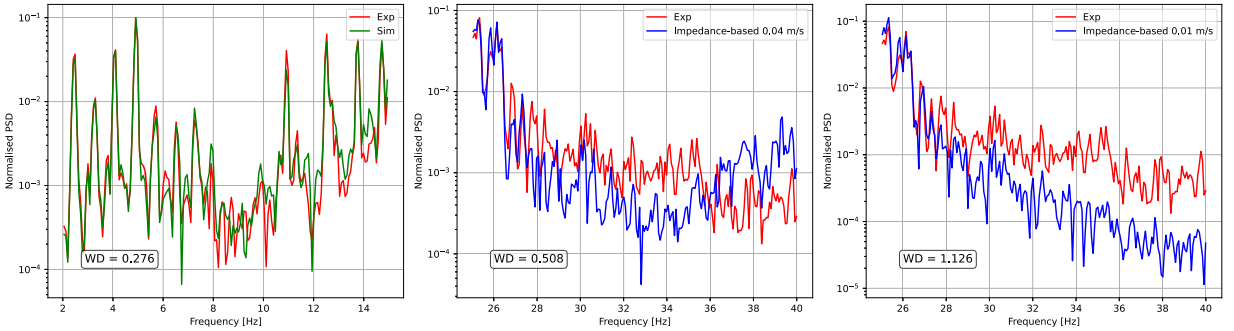

Fig. 25. Power spectral densities of the clamp force F_c for three selected cases from Table 5, illustrating how differences in the power spectral density shape across methods are reflected in the corresponding values of the Wasserstein distance index.

the power spectral densities were first band-limited to a chosen frequency band and normalised to unit area, transforming them into conventional distributions. A lower Wasserstein distance indicates better agreement, with a value of zero corresponding to perfect spectral overlap.

Table 5 summarises the Wasserstein distances between the experimental output power spectral density and those computed by the two methods for different frequency bands. Two amplitudes-$A_{\dot{y}_c} = 0.01$ and $A_{\dot{y}_c} = 0.04$ m/s-were used for the impedance-based approach. Since the input amplitude of the signal in Fig. 22 is closer to 0.04 m/s, this value yields better agreement, as reflected in the lower Wasserstein distances in Table 5. Within the 2-25 Hz range (where model parameters were identified), the full nonlinear model performs best. Beyond this range, however, the impedance-based method-when using an appropriate amplitude-can outperform the model. Fig. 25 shows three selected cases from Table 5 to give a visual representation of three different values of the Wasserstein distance index. The first case corresponds to the best agreement in the table and is obtained using the full nonlinear model within the range 2-15 Hz. In the second case, the comparison between the experimental normalised power spectral density and the impedance-based method at 0.04 m/s shows differences in the relative peak magnitudes, while in the third case-evaluated in the 25-40 Hz band using the impedance-based method-both the peak intensities and their locations deviate significantly from the experimental reference. This leads to a Wasserstein distance greater than one.

These results show that the full numerical model outperforms the impedance-based one if the input stays in the range where the model parameters were identified. Furthermore, the full numerical model is essential when the internal dynamics of the damper are required or when the input signal is not well characterised. Unlike the impedance-based method, it accommodates arbitrary input shapes and amplitudes and can be embedded into broader system-level simulations. Therefore, it eliminates the need to select a fixed input amplitude and offers better generalisation over a range of operating conditions.

What is particularly notable is that the nonlinear model was trained mode-by-mode using monoharmonic excitations, yet it is tested under multiharmonic field inputs and still succeeds in accurately reconstructing both the internal dynamics and the output force. The multiharmonic signals used for validation include frequency combinations that were not present during training, highlighting the generalisation capability and physical consistency of the proposed model. This outcome demonstrates the appropriateness of the proposed modelling approach and, importantly, shows that the identification process can remain relatively simple-relying only on monoharmonic inputs for calibration.

Finally, since the experimental impedance function is required to calibrate the nonlinear Bouc-Wen model, practitioners should be aware that both approaches-impedance-based and simulation-based-are complementary tools, and the choice between them should depend on the specific application and level of detail required.

4. Comparison with existing analytical models

The proposed multi-modal Bouc-Wen model for asymmetric Stockbridge dampers presented in Section 2.2, can be readily adapted to the symmetric case, in which the two masses are identical and the two messenger cables have the same length. This is done by enforcing the parameters for the top mass ($i = 1$) equal to the ones of the bottom mass ($i = 2$), with the only exception of the scaling parameters, which need to be set with opposite sign as $a_2 = -a_1$ and $b_2 = -b_1$, because of the different orientation of the two masses. This symmetry enables direct validation against existing formulations in the literature. We test our model on the experimental

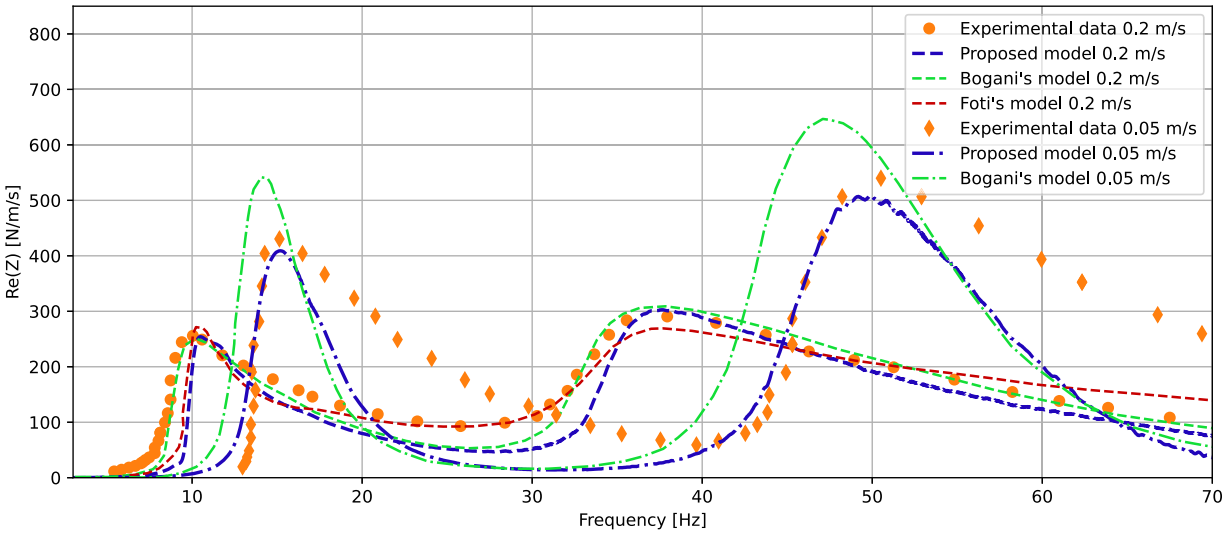

Fig. 26. Real part of the impedance function for a symmetric Stockbridge damper for two different constant clamp velocities. Comparison between the prediction of the proposed model and the models proposed by Bogani et al. [25] and Foti et al. [19]. The experimental data are from [18].

Table 6
Model parameters for the two degrees of freedom Bouc-Wen model tuned on literature experimental data from [18] of a symmetric Stockbridge.

	Top mass translation	Top mass rotation	Bottom mass translation	Bottom mass rotation
	$i=1$ $j=1$	$i=1$ $j=2$	$i=2$ $j=1$	$i=2$ $j=2$
$k_{ji}^{\min}$	3,700	50	3,700	50
$k_{ji}^{\max}$	12,000	165	12,000	165
c_{ji}	0.0011	0.0075	0.0011	0.0075
n	1	1	1	1
σ	1	1	1	1
a_i	0.001	–	–0.001	–
b_i	–	–10.5		10.5

Table 7
Geometric parameters of the Stockbridge damper tested by [18].

Parameter	Symbol	Value
Mass of top mass	m_1	0.856 [kg]
Mass of bottom mass	m_2	0.856 [kg]
Mass of clamp	m_c	0.050 [kg]
Rotational inertia of top mass (about centroid)	J_1	0.001814 [kg·m^2]
Rotational inertia of bottom mass (about centroid)	J_2	0.001814 [kg·m^2]
Distance from tip of messenger cable to centroid (top mass)	$e_{G,1}$	0.0325 [m]
Distance from tip of messenger cable to centroid (bottom mass)	$e_{G,2}$	0.0325 [m]
Length of messenger cable	L	0.1875 [m]

benchmark data set taken from [18], which provides the real part of the impedance function measured at two input amplitudes. The geometric parameters of the corresponding Stockbridge damper are summarised in Table 7. The parameters of the proposed model have been tuned for this comparison following the same procedure described in Section 3.3 and are reported in Table 6. The only difference with respect to the earlier tuning is that, in this case, an initial guess for the (two, rather than four) scaling parameters a and b was not available. The values of a_2 and b_2 reported in Table 4 were arbitrarily adopted as initial estimates, from which the iterative adjustment was performed. Here, we compare the real part of the impedance function defined in Eq. (15) with two other recent models presented in the literature by Foti et al. [19] and Bogani et al. [25]. Foti et al.'s model treats each messenger cable as an Euler-Bernoulli beam, with the sectional moment-curvature relation governed by a Bouc-Wen hysteresis model, whereas Bogani et al. [25] applies a global Bouc-Wen formulation similar in scope to the present work. However, in Bogani et al.'s approach, the equations of motion were written with respect to the messenger's tip displacement and rotation, the two hysteretic variables were identified as the displacement and rotation, and the inertial coupling between these two degrees of freedom was neglected. In terms of the present formulation, this corresponds to disregarding the $\eta_i e_{Gi} F_i$ term in Eq. (6b), and forcing a diagonal transformation matrix

($a_i = b_i = 0$). As a result, the two degrees of freedom were completely decoupled in their contribution to the impedance function, and the model parameters were identified by fitting one resonance peak at a time. In contrast, in the present work, no inertial contribution is disregarded, and the global Bouc-Wen model is applied in the space of generalised coordinates, allowing the coupled dynamics of all degrees of freedom to be consistently represented. Sauter and Hagedorn [18] also presented a sectional model using Masing-type hysteretic elements. However, as subsequent studies (e.g., Foti et al. [19]) have shown improved accuracy relative to the formulation of Sauter and Hagerdon, their model is not included in the present comparison to maintain clarity in the plots. These experimental data are the same as those used by both Bogani et al. and Foti et al. to validate their models. As shown in Fig. 26, the proposed model accurately reproduces the experimental impedance function for a clamp-velocity amplitude of 0.2 m/s, which was used for the tuning. Both the present model and Bogani et al.'s capture the amplitude-dependent variation of the dynamic response, a feature not demonstrated in Foti et al.'s original work. It should be noted that the results for Bogani et al.'s and Foti et al.'s models are taken directly from their respective publications and compared against the same experimental benchmark data, without any re-identification of parameters. Furthermore, while the proposed formulation can accommodate asymmetric dampers, when reduced to the symmetric case, it retains the same number of parameters as Bogani et al.'s model: six in total, with three associated with each degree of freedom of the masses. By contrast, Foti et al.'s model employs five parameters per cross section of the messenger cable, requiring identification for 11 sections in his study. Despite its generality, the proposed model therefore achieves comparable parametrisation to Bogani et al.'s while offering improved predictive accuracy, particularly at different clamp-velocity amplitudes than the ones used for tuning.

5. Conclusions

This study has presented a four-degree-of-freedom nonlinear model of an asymmetric Stockbridge damper designed for suspension bridge hangers. The model effectively captures the force transmitted by the damper to the hanger, providing a reliable representation of its external dynamic behaviour. Unlike black-box approaches, the proposed model also reproduces the internal dynamics of the damper masses with notable accuracy, offering valuable insight into their translational and rotational motion contributions.

In contrast to the state-of-practice, which relies on experimentally identified impedance functions at fixed input amplitudes, the proposed formulation offers a physically consistent representation that remains valid for arbitrary input histories. This enables the model to be directly embedded into larger dynamical simulations of hanger-damper systems.

A significant aspect of this work is the model's calibration using laboratory data collected from a damper unit sourced from the field installation on the Hålogaland Bridge. The tuning process utilised experimental impedance functions under varying input amplitudes to identify the hysteretic parameters of the Bouc-Wen formulation. This allowed the model to capture the amplitude-dependent nonlinearity that characterises the damper's performance.

To validate its robustness and accuracy, the model was tested using both sinusoidal excitations and time histories recorded in the field. These validation campaigns demonstrated that the model reliably predicts the transmitted force and the internal dynamics across a broad range of operating conditions and frequency content of the clamp motion.

Furthermore, the model was benchmarked against recent models from the literature developed for overhead power lines applications. Using the same experimental datasets employed to validate those models, the present formulation showed comparable and, in some cases, superior performance, especially in reproducing the amplitude-dependent shifts in the impedance function.

Future developments may focus on extending the formulation to predict the transmitted moment at the clamp, automating the parameter identification process based on families of experimental impedance functions, and evaluating the performance of the model once embedded in a full hanger-damper system and compared against long-term field measurements.

Overall, this work contributes an experimentally verified, nonlinear dynamic model capable of capturing both external force transmission and internal damper dynamics. It offers an improved tool for the design and assessment of Stockbridge dampers in bridge applications, with dimensions and installation conditions that are atypical for power line contexts.

CRediT authorship contribution statement

G. Bacci: Writing – original draft, Visualization, Validation, Software, Formal analysis, Data curation; **Ø.W. Petersen:** Writing – review & editing, Visualization, Supervision; **V. Denoël:** Supervision, Methodology, Conceptualization; **O. Øiseth:** Supervision, Project administration, Funding acquisition, Conceptualization.

Data availability

Data will be made available on request.

Declaration of competing interest

The authors declare that they have no known competing financial interests or personal relationships that could have appeared to influence the work reported in this paper.

Acknowledgement

This research was financially supported by the Norwegian Public Roads Administration. The authors appreciate this support.

Appendix A. Additional test results at different amplitudes

Standards for the application of Stockbridge dampers on overhead power lines recommend a clamp-velocity amplitude of $A_{\dot{y}_c} = 0.1$ m/s for forced-vibration shaker tests [3,4]. In contrast, no equivalent standard or recommended testing protocol exists for dampers intended for bridge hanger applications. The authors therefore selected the range of amplitudes to calibrate the present model from field observations on hangers equipped with Stockbridge dampers. The field measurements have been carried out on the Hålogaland bridge and described in [2]. Accordingly, the model parameters were fitted using data in the range $A_{\dot{y}_c} = 0.01$–0.05 m/s. Additional experiments were also performed at $A_{\dot{y}_c} = 0.1$ m/s. Fig. A1 shows the comparison between the experimental and numerical peak values of the modulus of the impedance function of the Stockbridge damper for different input velocity amplitudes. Relative to Fig. 18, the first point of each peak trajectory has been included in Fig. A1 and corresponds to $A_{\dot{y}_c} = 0.1$ m/s. The model continues to perform well, particularly for the first two resonances, even though this amplitude lies outside the parameter-identification range. Its accuracy in this case, therefore, represents an extrapolation of the trained model.

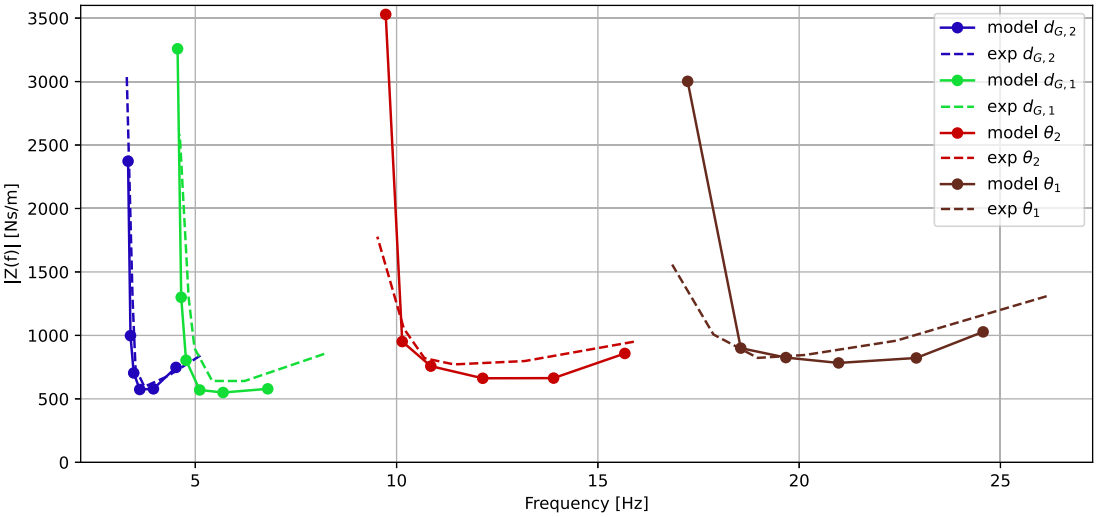

Fig. A1. Trajectories of the four peaks of the modulus of the impedance function of the Stockbridge damper, including $A_{\dot{y}_c} = 0.1$ m/s. The dashed line represents the experimental data, while the continuous line represents the tuned numerical Bouc-Wen model.

References

[1] A. Larsen, Vibration excitation and damping of suspension bridge hanger cables, in: V. Gattulli, M. Lepidi, L. Martinelli (Eds.), Dynamics and Aerodynamics of Cables. ISDAC 2023. Lecture Notes in Civil Engineering, Springer, Cham, 2024, pp. 217–227. https://doi.org/10.1007/978-3-031-47152-0{_}19
[2] G. Bacci, Ø. Petersen, V. Denoël, O. Øiseth, Advanced statistical analysis of vortex-induced vibrations in suspension bridge hangers with and without Stockbridge dampers, J. Wind Eng. Ind. Aerodyn. 255 (October) (2024) 105931. https://doi.org/10.1016/j.jweia.2024.105931
[3] N.E. Komite, EN IEC 61897:2020 - Overhead Lines Requirements and Tests for Aeolian Vibration Dampers, Technical Report, NEK, 2020.
[4] I.S. Committee, IEEE Guide for Laboratory Measurement of the Power Dissipation Characteristics of Aeolian Vibration Dampers for Single Conductors, Technical Report, IEEE, 1993.
[5] G.H. Stockbridge, Overcoming vibration in transmission cables, Electr. World 86.26 (1925) 1304–1306.
[6] R. Claren, G. Diana, Mathematical analysis of transmission line vibration data, IEEE Trans. Power Appar. Syst. 88 (12) (1969). https://doi.org/10.1016/0378-7796(78)90013-5
[7] J. Chan, D. Havard, C. Rawlins, G. Diana, L. Cloutier, J. Lilien, C. Hardy, J. Wang, A. Goel, EPRI transmission line reference book: wind-induced conductor motion, Electric Power Research Institute (EPRI), 2009, 4–130.
[8] H. Wagner, V. Ramamurti, R.V.R. Sastry, K. Hartmann, Dynamics of Stockbridge dampers, J. Sound Vib. 30 (2) (1973) 207–220. https://doi.org/10.1016/S0022-460X(73)80114-2
[9] N. Barbieri, R. Barbieri, Dynamic analysis of Stockbridge damper, Adv. Acoust. Vib. 2012 (2012). https://doi.org/10.1155/2012/659398
[10] G. Diana, A. Cigada, M. Belloli, M. Vanali, Stockbridge-type damper effectiveness evaluation: part I - Comparison between tests on span and on the shaker, IEEE Trans. Power Delivery 18 (4) (2003) 1462–1469. https://doi.org/10.1109/TPWRD.2003.817797
[11] G. Diana, A. Manenti, C. Pirotta, A. Zuin, Stockbridge-type damper effectiveness evaluation: part II - The influence of the impedance matrix terms on the energy dissipated, IEEE Trans. Power Delivery 18 (4) (2003) 1470–1477. https://doi.org/10.1109/TPWRD.2003.817798
[12] N. Carpineto, W. Lacarbonara, F. Vestroni, Hysteretic tuned mass dampers for structural vibration mitigation, J. Sound Vib. 333 (5) (2014) 1302–1318. https://doi.org/10.1016/j.jsv.2013.10.010
[13] I. Pivovarov, O.G. Vinogradov, One application of Bouc's model for non-linear hysteresis, J. Sound Vib. 118 (2) (1987) 209–216. https://doi.org/10.1016/0022-460X(87)90521-9
[14] R. Bouc, Modele mathematique d'hysteresis, Acustica 21 (1971) 16–25.
[15] Y.-K. Wen, Method for random vibration of hysteretic systems, J. Eng. Mech. Div. 102.2 (1976) 249–263.
[16] F. Foti, L. Martinelli, An analytical approach to model the hysteretic bending behavior of spiral strands, Appl. Math. Model. 40 (2016) 6451–6467. https://doi.org/10.1016/j.apm.2016.01.063
[17] D. Sauter, P. Hagedorn, On the hysteresis of wire cables in Stockbridge dampers, Int. J. Non Linear Mech. 37 (8) (2002) 1453–1459. https://doi.org/10.1016/S0020-7462(02)00028-8
[18] D. Sauter, Modeling the dynamic characteristics of slack wire cables in Stockbridge dampers, Ph.D. thesis, Technischen Universität Darmstadt, 2003.

[19] F. Foti, L. Martinelli, Hysteretic behaviour of Stockbridge dampers: modelling and parameter identification, Math. Prob. Eng. 2018 (2018). https://doi.org/10.1155/2018/8925121
[20] S. Langlois, F. Legeron, Prediction of Aeolian vibration on transmission-line conductors using a nonlinear time history model - Part I: damper model, IEEE Trans. Power Delivery 29 (3) (2014) 1168–1175. https://doi.org/10.1109/TPWRD.2013.2291361
[21] N. Barbieri, R. Barbieri, R.A. da Silva, M.J. Mannala, B.L. de Sant'Anna Vitor, Nonlinear dynamic analysis of wire-rope isolator and Stockbridge damper, Nonlinear Dyn. 86 (1) (2016) 501–512. https://doi.org/10.1007/s11071-016-2903-1
[22] N. Barbieri, M.E. Marchi, M.J. Mannala, R. Barbieri, B.L. de Sant'Anna Vitor, B.G. de Sant'Anna Vitor, Nonlinear dynamic analysis of a Stockbridge damper, Can. J. Civ. Eng. 46 (9) (2019) 828–835. https://doi.org/10.1139/cjce-2018-0502
[23] X. Luo, L. Wang, Y. Zhang, Nonlinear numerical model with contact for Stockbridge vibration damper and experimental validation, JVC/J. Vib. Contr. 22 (5) (2016) 1217–1227. https://doi.org/10.1177/1077546314535647
[24] F. Foti, V. Denoël, L. Martinelli, F. Perotti, A stochastic and continuous model of Aeolian vibrations of conductors equipped with Stockbridge dampers, Proc. Int. Conf. Struct. Dyn., EURODYN 1 (2020) 2088–2102. https://doi.org/10.47964/1120.9169.20304
[25] F. Bogani, A. Sosio, F. Foti, L. Martinelli, A reduced hysteretic model of Stockbridge dampers, Theor. Appl. Mech. - AIMETA 2022 26 (2023) 417–422. https://doi.org/10.21741/9781644902431-68
[26] F. Di, L. Sun, L. Qin, L. Chen, Y. Zou, L. Jiang, Y. Zhu, Full-scale experimental study on vibration control of bridge suspenders using the Stockbridge damper, J. Bridge Eng. 25 (8) (2020) 1–10. https://doi.org/10.1061/(asce)be.1943-5592.0001591
[27] F. Di, L. Sun, L. Chen, Suppression of vortex-induced high-mode vibrations of a cable-damper system by an additional damper, Eng. Struct. 242 (2021) 112495. https://doi.org/10.1016/j.engstruct.2021.112495
[28] A. Olosz, B. Kövesdi, P. Hegyi, L. Dunai, Improvement of stockbridge damper design for cable-stayed bridges, Appl. Mech. 5 (4) (2024) 818–838. https://doi.org/10.3390/applmech5040046
[29] M. Markiewicz, Optimum dynamic characteristics of Stockbridge dampers for dead-end spans, J. Sound Vib. 188 (2) (1995) 243–256. https://doi.org/10.1006/jsvi.1995.0589
[30] F. Bogani, S. Alex, Modellazione di dissipatori Stockbridge per la mitigazione delle vibrazioni eoliche dei cavi sospesi, Ph.D. thesis, Politecnico di Milano, 2021. https://hdl.handle.net/10589/182363.
[31] A. Bedford, Hamilton's Principle in Continuum Mechanics, Springer International Publishing, Cham, Cham, 1985. https://doi.org/10.1007/978-3-030-90306-0
[32] A.E. Charalampakis, V.K. Koumousis, Identification of Bouc-Wen hysteretic systems by a hybrid evolutionary algorithm, J. Sound Vib. 314 (3–5) (2008) 571–585. https://doi.org/10.1016/j.jsv.2008.01.018
[33] J. Song, A. Der Kiureghian, Generalized Bouc-Wen model for highly asymmetric hysteresis, J. Eng. Mech. 132 (6) (2006) 610–618. https://doi.org/10.1061/(ASCE)0733-9399(2006)132:6(610)
[34] A.E. Charalampakis, Parameters of Bouc–Wen hysteretic model revisited, Proceedings of the 9th HSTAM International Congress on Mechanics, (2010).
[35] F. Ikhouane, J. Rodellar, J.E. Hurtado, Analytical characterization of hysteresis loops described by the Bouc-Wen model, Mechanics of Advanced Materials and Structures 13 (6) (2006) 463–472. https://doi.org/10.1080/15376490600862830
[36] F. Ikhouane, V. Mañosa, J. Rodellar, Dynamic properties of the hysteretic Bouc-Wen model, Syst. Contr. Lett. 56 (3) (2007) 197–205. https://doi.org/10.1016/j.sysconle.2006.09.001
[37] Ø. Petersen, G.T. Frøseth, O. Øiseth, Design and deployment of a monitoring system on a long-span suspension bridge, in: Proceedings of the International Conference on Structural Health Monitoring of Intelligent Infrastructure, 2021-June, 2021, pp. 1813–1817.
[38] S. Kolouri, S.R. Park, M. Thorpe, D. Slepcev, G.K. Rohde, Optimal mass transport: signal processing and machine-learning applications, IEEE Signal Process. Mag. 34 (4) (2017) 43–59. https://doi.org/10.1109/MSP.2017.2695801
[39] SciPy, scipy.stats.wasserstein_distance - SciPy v1.11.0 Manual, 2025, https://docs.scipy.org/doc/scipy/reference/generated/scipy.stats.wasserstein_distance.html#rbc4e517f9be6-1.